2

Forest Structure Retrieval from Multi-Baseline SARs

Stefano Tebaldini
Politecnico di Milano
Italy

1. Introduction

The vertical structure of the forested areas has been recognized by the scientific community as one major element in the assessment of forest biomass. Dealing with a volumetric object, the remote sensing techniques that are best suited to infer information about the forest structure are those that guarantee under foliage penetration capabilities. One important, widely popular technology used to investigate the forest vertical structure from the above (typically on board aircrafts) is given by high resolution LIDAR (Light Detection and Ranging) sensors, whose signals penetrate down to the ground trough the gaps within the vegetation layer. In the recent years, however, the attention of the scientific community has been drawn by the use of SAR (Synthetic Aperture Radar) techniques. As opposed to LIDARs, for which high resolution is crucial, the signals emitted by SARs propagate down to the ground by virtue of the under foliage penetration capabilities of microwaves. This different way of sensing the volumetric structure of the imaged objects determines many peculiarities of SAR imaging with respect to LIDAR, some of which are advantages and other drawbacks. The most remarkable advantage is perhaps the one due to the ability of microwaves to penetrate into semi-transparent media, which makes lower wavelength (L-Band and P-Band, typically) SARs capable of acquiring data almost independently of weather conditions and vegetation density. Conversely, the most relevant drawback is that the three dimensional (3D) reconstruction of the imaged objects requires the exploitation of multiple (at least two, but preferable many) images acquired from different points of view, and hence multiple passes over the scene to be investigated.

The aim of this chapter is to discuss relevant topics associated with the employment of a multi-baseline SAR system for the reconstruction of the 3D structure of the imaged targets, with particular attention to the case of forested areas.

The first topic considered is the design of a multi-baseline SAR system for 3D reconstruction in the framework of Fourier Tomography (FT), also referred to as 3D focusing. Even though seldom used in practical applications due to poor imaging quality, FT allows to discuss quite easily the design and overall features of a SAR tomographic system, and represents the basis for all of the developments presented in the remainder of this chapter.

The next part of this chapter will focus on operative methods the generation of high-resolution tomographic imaging from sparse data-sets. This is the case of interest in practical applications, due to the costs associated with flying a high number of passes and platform trajectory accuracy. T-SAR will be cast here in terms of an estimation problem, considering both non-parametric and parametric, or model based, approaches. Non-parametric

approaches provide enhanced resolution capabilities without the need for a-priori information about the targets. Model based approaches are even more powerful, providing access to a quantitative, large scale characterization of the forest structure. Nevertheless, model based approaches are affected by an intrinsic limitation, in that data interpretation can be carried out only on the basis of the model that has been adopted.
The final part of this chapter will focus on the joint exploitation of multi-polarimetric and multi-baseline data. It will be shown that under large hypotheses the second-order statistics of such data can be expressed as a Sum of Kronecker Products (SKP), which provides the basis to proceed to decomposing the SAR data into ground-only and volume-only contributions even in absence of a parametric model. Furthermore, the SKP formalism will be shown to provide a compact representation of all physically valid and data-consistent two-layered models. Such a feature will be exploited to provide a exhaustive discussion about the validity of such a class of models for forestry investigation.
Different case studies will be discussed throughout the whole chapter, basing on real data-sets from the ESA campaigns BIOSAR 2007, BIOSAR 2008, and TROPISAR.

2. SAR tomography

2.1 SAR imaging principles

RADAR (Radio Detection And Ranging) is a technology to detect and study far off targets by transmitting ElectroMagnetic (EM) pulses at radio frequency and observing the backscattered echoes. In its most simple implementation, a Radar "knows" the position of a target by measuring the delay of the backscattered echo. Delay measurements are then converted into distance, or range, measurements basing on the wave velocity in the medium (most commonly free space is assumed). Range resolution, $\triangle\, r$, is then directly related to the bandwidth of the transmitted pulse according to well known relation:

$$\triangle\, r = \frac{c}{2B} \tag{1}$$

where c is the speed of light and B the signal bandwidth.
A Synthetic Aperture Radar (SAR) system is constituted, in its essence, by a Radar mounted aboard a moving platform, such as an aircraft or a satellite. As the platform moves along its trajectory, the Radar mounted aboard transmits pulse waveforms at radio-frequency and gathers the echoes backscattered from the scene. The ensemble of the echoes recorded along the track is generally referred to as raw data, meaning that this product is not, in most cases, directly interpretable in terms of features of the illuminated scene. This happens because of the small size of the antennas usually employed by SAR sensors (few meters as order of magnitude), which results in a significantly large beam on the ground. As a consequence, each recorded echo is determined by a very large number of targets, widely dispersed along the scene. The procedure through which it is possible to separate the contributions of the targets within the Radar beam is generally referred to as SAR focusing. Such a procedure consists in combining the echoes collected along the platform track so as to *synthesize* a much longer antenna than the real one, typically ranging from tens of meters in the airborne case to tens of kilometers in the spaceborne case, and narrow the beam width on the ground to few meters. After focusing, the contribution of each target is identified by two coordinates, as shown in see Fig. (1). The first one, conventionally named azimuth, may be though of as the projection of the platform track onto the Earth's surface. The other, conventionally named slant range, denotes the distance from the platform track at any given azimuth location. The

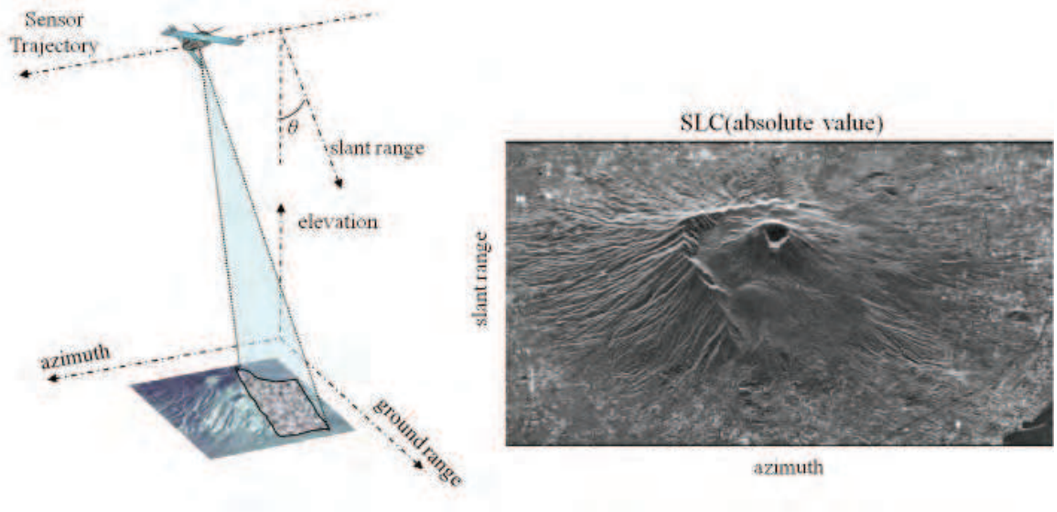

Fig. 1. SAR acquisition geometry.

result is a complex 2D signal indexed by the slant range, azimuth coordinates, usually referred to Single Look Complex (SLC) image.
Assuming a narrow bandwidth signal the azimuth resolution, $\triangle x$, can be obtained as:

$$\triangle x = \frac{\lambda}{2L_s} r \tag{2}$$

where λ is the carrier wavelength, L_s is the length of the synthetic aperture, and r is the stand-off distance between the sensor and the target. Slant range resolution is obtained according to eq. (1). A further description of SAR image formation is beyond the scopes of this chapter. For further details, the reader is referred to (1), (2), (3), (4).

2.2 3D SAR imaging

Given the definitions above, a SAR SLC image represents the scene as projected onto the slant range, azimuth coordinates. This entails the complete loss of the information about the third dimension, i.e.: about the vertical structure of the targets within the imaged scene. The key to the recovery of the third dimension is to enhance the acquisition space so as to form a *further* synthetic aperture. The easiest way to do this is to employ a multi-baseline SAR system, where several SAR sensors, flown along parallel tracks, image the scene from different points of view, see figure (2).
Such a system offers the possibility to gather the backscattered echoes not only along the azimuth direction, but also along the cross-range direction, defined by the axis orthogonal to the Line Of Sight (LOS) and to the orbital track. Accordingly, the backscattered echoes can be focused not only in the slant range, azimuth plane, but in the whole 3D space. Therefore, the exploitation of multi-baseline acquisitions allows to create a fully 3D imaging system, where the size of the 3D resolution cell is determined by the pulse bandwidth along the slant range direction, and by the lengths of the synthetic apertures, according to eq. (2), in the azimuth and cross range directions, see Fig. (3).
Both 2D and 3D SAR imaging data may be regarded as specializations to the SAR case of the more general concept of Diffraction Tomography, widely exploited in seismic processing (5). As such, 3D focusing is analogous to the basic formulation of SAR Tomography (T-SAR), in which no particular assumption is adopted to describe the imaged scene (6).

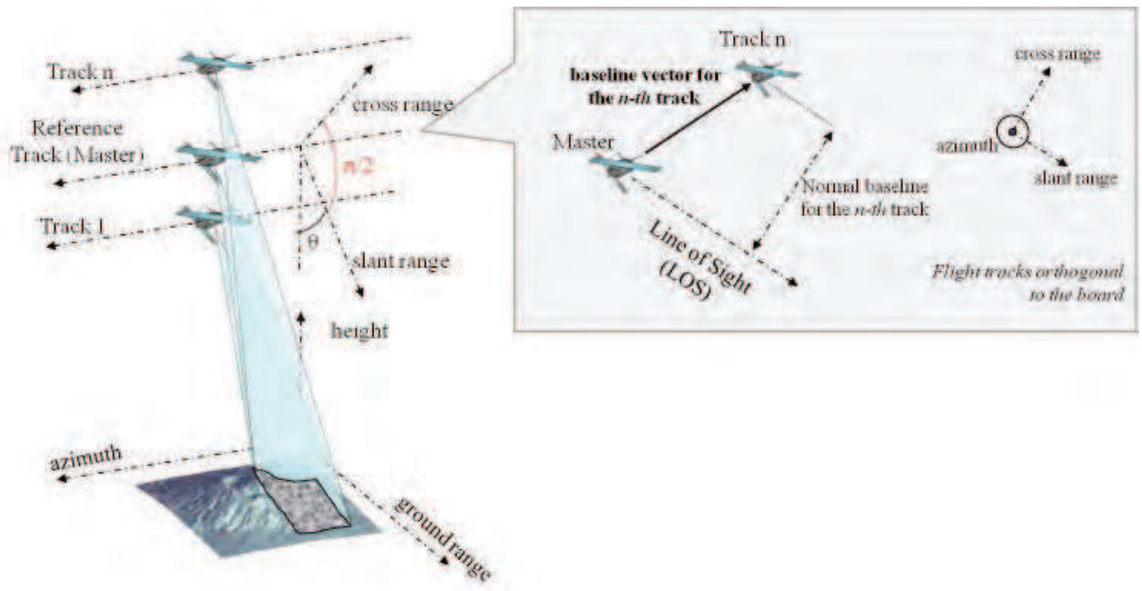

Fig. 2. A multi-baseline SAR system

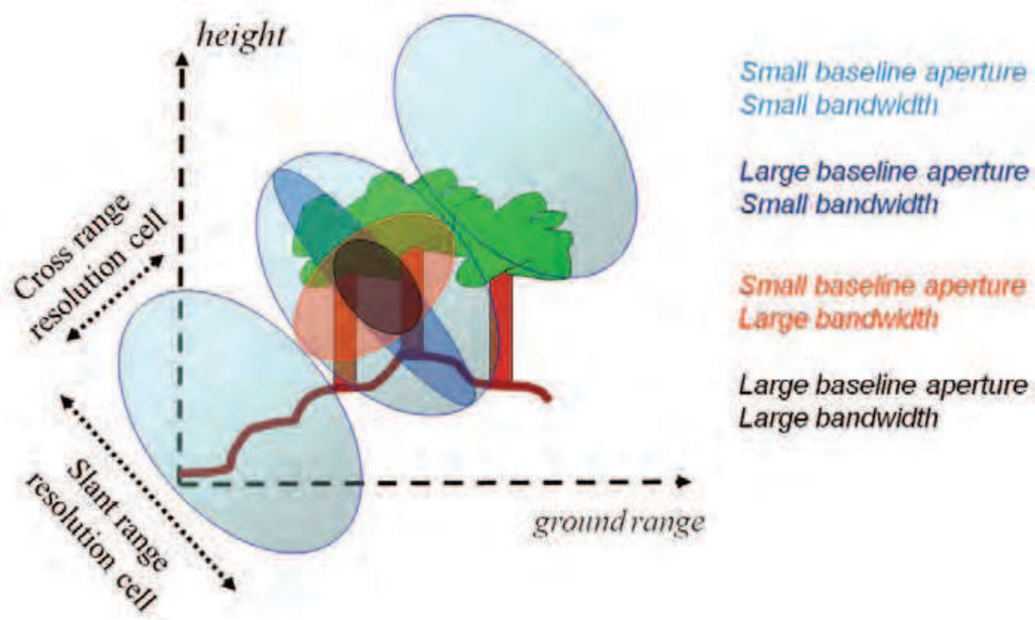

Fig. 3. Section of the 3D resolution cell in the slant range, cross range plane, represented as a function of baseline aperture and pulse bandwidth.

2.3 SAR tomography: mathematical formulation

Consider the case of a multi-baseline data-set, represented by N Single Look Complex (SLC) monostatic SAR images, properly co-registered and phase flattened (7). Let y_n denote a complex valued pixel in the $n-th$ image, the dependence on the slant range, azimuth location, (r, x), being made implicit in order to simplify the notation. After (7), each acquisition can be expressed through the following forward model:

$$y_n = \int h\left(r', x'\right) s\left(r', x', \xi'\right) \exp\left(j\frac{4\pi}{\lambda r} b_n \xi'\right) dr' dx' d\xi' \tag{3}$$

where: (r', x') are the slant range, azimuth coordinates with respect to the center of the SAR resolution cell; ξ' is the cross range coordinate with respect to the center of the SAR resolution cell, given by the axis orthogonal to (r', x'); $s\left(r', x', \xi'\right)$ is a the scene complex reflectivity, namely a complex valued quantity accounting for amplitude and phase modifications due to the interactions of the transmitted pulse with each of the scatterers within the SAR resolution cell; $h\left(r', x'\right)$ is the end-to-end SAR impulse response (after focusing); b_n is the normal baseline relative to the $n-th$ image with respect to a common master image.
Resolving the integral in (3) with respect to (r', x'), one gets:

$$y_n = \int P\left(\xi'\right) \exp\left(j\frac{4\pi}{\lambda r} b_n \xi'\right) d\xi' \tag{4}$$

where

$$P\left(\xi'\right) = \int h\left(r', x'\right) s\left(r', x', \xi'\right) dr' dx' \tag{5}$$

is the target projection within the SAR resolution cell along the cross-range coordinate. Equation (4) may be thought of as the key equation of T-SAR. It states that the SAR data and the target projections form a Fourier pair. Hence, the cross-range distribution of the backscattered power, namely

$$S_{\xi}\left(\xi\right) = E\left[\left|P\left(\xi\right)\right|^2\right], \tag{6}$$

can be retrieved by estimating the Fourier Spectrum (FS) of the data with respect to the normal baselines. The evaluation of (6) for every slant range, azimuth location results in a 3D reconstruction of the imaged scene, in the coordinate system defined by the slant range, azimuth, cross-range coordinates. Accordingly, the vertical distribution of the backscattered power can be retrieved by re-sampling the reconstructed scene from the slant range, azimuth, cross-range coordinates to the ground range, azimuth, elevation coordinates. For sake of simplicity, in this paper I will suppose that the passage from the cross-range coordinate, ξ, to elevation, z, can be simply described through the equation

$$\xi = z/\sin\theta \tag{7}$$

where θ is the look angle. Under this assumption, the vertical distribution of the backscattered power can be obtained from the FS simply as $S\left(z\right) = S_{\xi}\left(\xi = z/\sin\theta\right)$. Notice that such a simplification does not entail any loss of generality, as the exact reconstruction of the vertical backscattered power at every ground range, azimuth location can be carried out a-posteriori through simple geometrical arguments.

2.4 Expected FS for forested areas

A brief discussion is now required about the physics of radar scattering from forested areas, in order to discuss the expected properties of the FS. Many excellent works have been done on modeling radar backscattering for forested areas, see for example (8), (9), (10). After these works, forested areas will be characterized as the ensemble of trunks, canopies, intended as the ensemble of leaves and branches, and terrain. A simple and widely exploited solution to describe the scattering behavior of a target above the ground is provided by modeling the ground as a flat half space dielectric and using image theory. Four Scattering Mechanisms arise by retaining this approach (11), (12), (9): backscatter from the target; target to ground double bounce scattering; ground to target double bounce scattering; backscatter from the target illuminated by the reflected wave, namely ground to target to ground scattering. In the following the contributions from ground to target to ground scattering will be assumed to be negligible. In the case of trunks, this assumption is supported by considering that backscatter is dominated by specular scattering, and may thus be neglected (9). For the same reason, direct backscatter from the trunks will be neglected as well. The case of the canopy is a little more delicate, since randomly oriented small objects such as branches and leaves should be treated as isotropic scatterers. Also in this case, however, it makes sense to retain that ground to target to ground contributions may be neglected, by virtue of the attenuation undergone by the wave as it bounces on the ground and propagates through the trunk layer and the canopy layer of adjacent trees.

Accordingly, higher order multiple scattering will be neglected as well. As for double bounce scattering, through simple geometric arguments it is possible to see that the distance covered by the wave as it undergoes the two consecutive specular reflections on the ground and on the target, or viceversa, is equal to the distance between the sensor and the projection of the target onto the ground. Therefore, at least on an approximately flat terrain, every double bounce mechanism is located on the ground. Assuming that trees grows perfectly vertical, the projection of the trunk onto the ground collapses into a single point. Hence, double bounce scattering due to trunk-ground interactions may be regarded as a point-like scattering mechanism, located on the ground. The projection of the canopy onto the ground, instead, gives rise to a superficial scattering mechanism located on the ground, analogous to ground backscatter[1].

Based on the model here discussed, a forest scenario is to be characterized, from the point of view of a SAR based analysis, as an ensemble of point like, superficial and volumetric scatterers. Basing on single polarimetric, multi-baseline observations, the element of diversity among the different Scattering Mechanisms (SMs) is given by their corresponding FS, see Fig. (4). Trunk-ground interactions give rise to a point-like SM whose phase center is ground locked, resulting in an isolated narrow peak in the associated FS, located at ground level. Ground backscatter and canopy-ground interactions give rise to a superficial, ground locked, SM. It follows that the associated FS is located at ground level as well, but it is spread along the cross-range axis. Canopy backscatter gives rise to a volumetric SM whose phase center is located above the ground, depending on canopy height, from which it follows that the associated FS is located above the ground, and it is spread along the cross-range axis as well.

2.5 Baseline design

After equation (4), the design of the baseline set for tomographic application may be performed basing on standard results from Signal Theory (14). In particular, as the aim is

[1] It has to be remarked that these conclusions do not apply in the case of bi-static acquisitions, see for example (13)

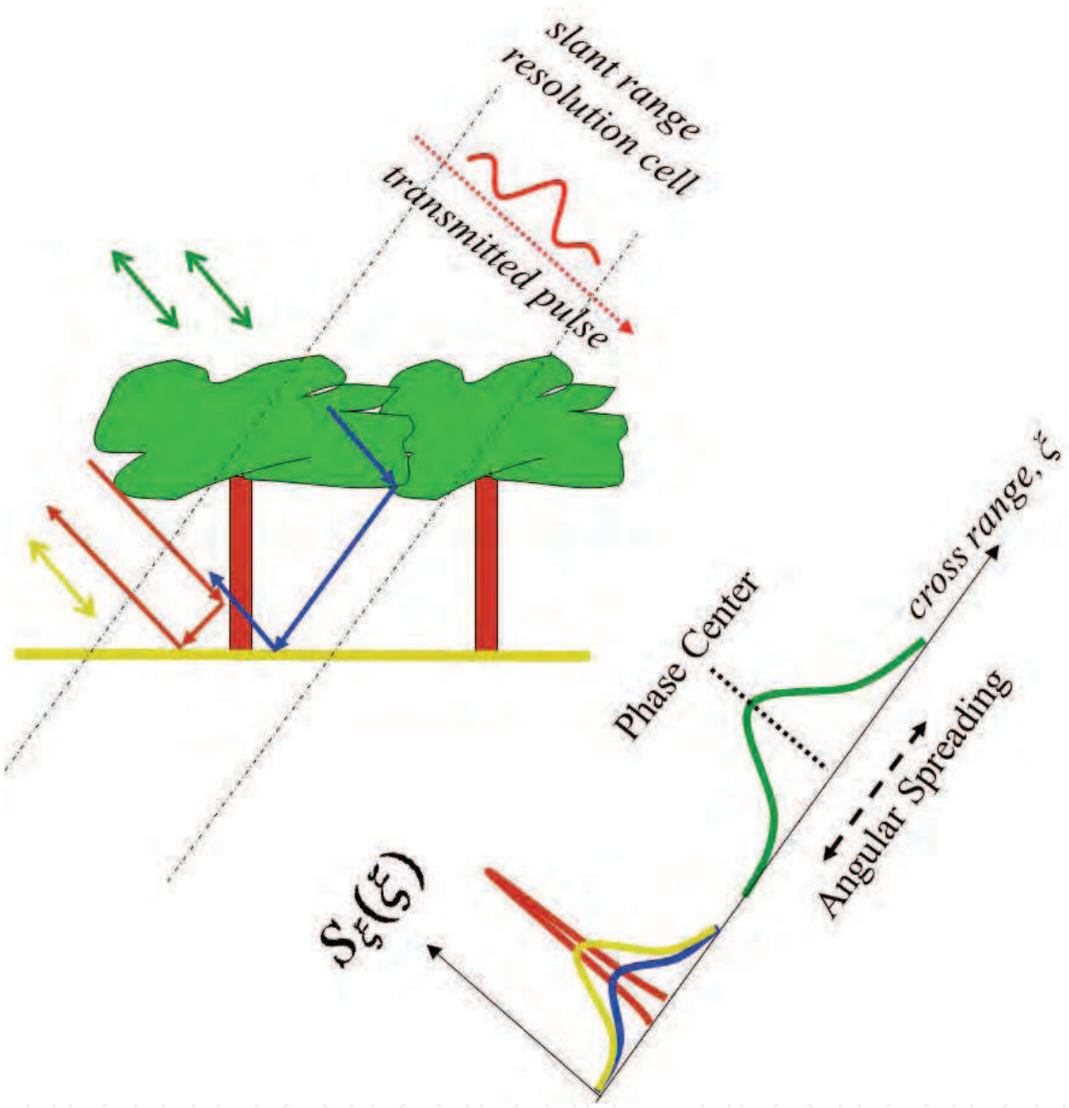

Fig. 4. Pictorial representation of the Fourier Spectra associated to the four scattering mechanisms discussed. Brown: Trunk-ground scattering; yellow: ground backscattering; green: canopy backscattering; blue: canopy-ground scattering.

to correctly represent the power spectrum of the data, the baseline set has to be designed in such a way as to avoid the arising of aliasing phenomena while allowing a sufficient resolution. As discussed above, equation (4) states that, at each slant range azimuth location, the complex valued pixel y_n associated with the $n-th$ baseline is obtained by taking the spectral component of target projection corresponding to the spatial frequency:

$$f_n = \frac{2b_n}{\lambda r} \tag{8}$$

Assume now that baseline sampling is uniform with baseline spacing $\triangle b$, i.e.: $b_n = n\triangle b$. It then follows that the reconstruction of $P(\xi)$ from y_n is unambiguous only provided that the overall extent of the target along the cross-range direction, H_{ξ}, is lower than the inverse of the frequency spacing, i.e.: $H_{\xi} \leq \frac{1}{\triangle f} = \frac{\lambda r}{2\triangle b}$. After fig. (4) it is immediate to see that:

$$H_{\xi} = \frac{H}{\sin\theta} + \triangle r\cos\theta \tag{9}$$

where H is forest height. Accordingly, the fundamental constraint to obtain a correct tomographic imaging of a forest is that[2]:

$$\frac{H}{\sin\theta} + \triangle r\cos\theta \leq \frac{\lambda r}{2\triangle b} \tag{10}$$

which allows to set the baseline spacing as a function of forest height and system features.
Cross range system resolution can be derived analogously to 2, simply by noting that the overall extent of the synthetic aperture in the cross direction is given by $N\triangle b$, N being the total number of tracks. Accordingly:

$$\triangle \xi = \frac{\lambda r}{2N\triangle b} \tag{11}$$

after which vertical resolution is written immediately as:

$$\triangle z = \frac{\lambda r}{2N\triangle b}\sin\theta. \tag{12}$$

Accordingly, the number of tracks is directly related to the vertical resolution of the tomographic system. Put in these terms, one would be tempted to assume that vertical resolution can be improved at will, simply by allowing a sufficient number of tracks. There are factors, though, which pose an upper limit about baseline aperture:

- if different baselines are collected at different times it has to be considered that the scene can undergo significant changes, resulting in the impossibility to coherently combine different images. This phenomenon is known in literature as temporal decorrelation (15), (16).
- It is important to keep in mind that equation (3) is valid upon the condition that the scene reflectivity is isotropic. This condition generally holds for narrow-angle (i.e.: small baseline) measurements, whereas it tends to break down in case of wide-angle measurements.
- Gathering multiple baselines is, in general, associated with high costs, due to the necessity to use multiple SAR sensors or fly the same sensor many times.

3. SAR Tomography as an estimation problem

Despite being a most powerful tool for system design, casting T-SAR in terms of a simple evaluation of the data Fourier Transform constitutes too simple an approach for practical applications. The main reason for this statement is that the capability to resolve

[2] This formula is given for typical geometries used in SAR imaging, where the incidence angle is usually larger than, say, 25°. The case of nadir looking Radar ($\theta = 0$) is not considered here.

targets in different positions through this simple approach is dramatically limited by the effective baseline aperture, according to equation (12). Furthermore, the vertical backscatter distribution that is yielded by Fourier based T-SAR is likely to be affected by the presence of grating lobes, that can arise in case of uneven baseline sampling (17). It follows that T-SAR can be more effectively posed as the problem of estimating the vertical distribution of the backscattered power based on a limited number of observations, that is as a Spectral Estimation problem. Many excellent works have appeared in literature about the application of spectral estimation methods to SAR tomography. A possible solution to improve the vertical resolution and ease the arising of side lobes is to exploit super-resolution techniques developed in the Direction of Arrival (DOA) framework, such as Capon adaptive filtering, MUSIC, SVD analysis, Compressive Sensing, and others. In the framework of T-SAR, such techniques have been applied in a number of works, among which (17), (18), (19), (20). The main limitation of most super-resolution techniques derives from the assumption that the scene is constituted by a finite number of point-like scatterers, which hinders their application in the analysis of scenarios characterized by the presence of distributed targets. For this reason, super-resolution techniques appear to be mainly suited for the tomographic characterization of urban areas. A different solution may be found in the works by *Fornaro et al.*, (21), (22), focused on the analysis of urban areas, and in those relative to Polarization Coherence Tomography (PCT), due to *Cloude*, (23), (24), focused on the analysis of forested areas. The common trait of those works is that super-resolution is achieved by exploiting a priori information about target location. In the case of forested areas, for example, the a priori information is represented by ground topography and canopy top height.
Alternatively, a sound characterization of the imaged scene can be given by modeling its vertical backscattering distribution, in such a way as to pose T-SAR as a Parametric Estimation problem. Model based techniques have been successfully employed in a number of works about the analysis of forested areas, see for example (25), (13), (26), (27). Nevertheless, model based approaches are affected by an intrinsic limitation, in that data interpretation can be carried out only on the basis of the model that has been adopted.

3.1 Two simple spectral estimators

Spectral estimation techniques are mostly based on the analysis of the data covariance matrix among different tracks, namely the matrix whose elements are obtained as:

$$\{\mathbf{R}\}_{nm} = E\left[y_n y_m^*\right] \tag{13}$$

The most simple estimator of the scene backscatter distribution is given by the Periodogram, which is defined as:

$$S_p\left(\xi\right) = \mathbf{a}\left(\xi\right)^T \widehat{\mathbf{R}}\mathbf{a}\left(\xi\right) \tag{14}$$

where $\widehat{\mathbf{R}}$ is the sample estimate of the data covariance matrix defined above and $\mathbf{a}\left(\xi\right) = \left[\exp\left(j\frac{4\pi}{\lambda r}b_1\xi\right) \cdots\cdots \exp\left(j\frac{4\pi}{\lambda r}b_N\xi\right)\right]^H$. The Periodogram is formally equivalent to the Fourier transform of the data with respect to the normal baseline. The vertical resolution provided by such an estimator is then given by eq. (12).
This limit may be overcome by adaptive filtering techniques. Capon filtering, for example, designs a filter $\mathbf{f}_{\min}$ such that:

$$\mathbf{f}_{\min} = \arg\min\left\{\mathbf{f}^H\widehat{\mathbf{R}}\mathbf{f}\right\} \tag{15}$$

under the linear constraint

$$\mathbf{f}^H\mathbf{a}\left(\xi\right) = 1 \tag{16}$$

This leads to the definition of the Capon Spectral Estimator as:

$$S_C(\xi) = \mathbf{f}_{\min}^H \widehat{\mathbf{R}} \mathbf{f}_{\min} = \frac{1}{\mathbf{a}(\xi)^H \widehat{\mathbf{R}}^{-1} \mathbf{a}(\xi)} \tag{17}$$

Such an estimator produces super-resolution capabilities and grating lobes reduction without the need for a-priori information about the targets, see for example (17), (18). The main drawback associated with the Capon Spectral Estimator is the poor radiometric accuracy, especially in presence of a small baseline aperture. Accordingly, the employment of the Capon Spectral Estimator has to be considered as a compromise. Indeed it results in non accurate backscattered power values, yet it permits to appreciate details that could not be accessible in presence of a small baseline aperture.

3.2 Representation of multiple SMs

Dealing with natural scenarios, it is sensible to assume that the target signature changes randomly from one pixel to another, either in the case of distributed or point-like targets. For this reason, the data will be assumed to be a realization of a zero-mean complex process, from which it follows that a unified mathematical treatment of all the SMs described in section 2.4 may be provided by characterizing the second order moments of the data, represented by the expected value of the interferograms. Under the hypothesis of statistical uncorrelation among the different SMs, the expected value of the $nm-th$ interferogram may be expressed as:

$$E[y_n y_m^*] = \sum_{k=1}^{K} \sigma_k^2 \gamma_{nm}^{(k)} \tag{18}$$

where: K is the total number of SMs; σ_k^2 is the backscattered power associated to the $k-th$ SM; $\gamma_{nm}^{(k)}$ is the complex interferometric coherence induced by the spatial structure (i.e.: point-like, superficial, or volumetric) associated with the $k-th$ SM in the $nm-th$ interferogram (15). After (18), the expression of the data covariance matrix is given by:

$$E\left[\mathbf{y}_{MB}\mathbf{y}_{MB}^H\right] \stackrel{def}{=} \mathbf{R} = \sum_{k=1}^{K} \sigma_k^2 \mathbf{R}_k \tag{19}$$

where: $\mathbf{y}_{MB} = \left[y_1\ y_2 \cdots y_N\right]^T$ is the stack of the multi-baseline data at a certain slant range, azimuth location; each matrix $\mathbf{R}_k$ is an $N \times N$ matrix whose entries are given by the interferometric coherences associated to the $k-th$ phase center: $\{\mathbf{R}_k\}_{nm} = \gamma_{nm}^{(k)}$. The role of each matrix $\mathbf{R}_k$ in (19) is to account for the spatial structure associated to each SMs. According to this interpretation, such matrices will be hereinafter referred to as *structure matrices*.

Following the arguments presented in section 2.4, the data covariance matrix will be assumed to be contributed by just two SMs, one associated with volume backscattering, and the other with the ensemble of all SMs whose phase center is ground locked, namely surface backscattering, ground-volume scattering, and ground-trunk scattering. Accordingly, eq. (19) simplifies to:

$$E\left[\mathbf{y}_{MB}\mathbf{y}_{MB}^H\right] \stackrel{def}{=} \mathbf{R} = \sigma_g^2 \mathbf{R}_g + \sigma_v^2 \mathbf{R}_v \tag{20}$$

the subscripts g, v standing for *ground* and *volume*.

3.3 A simple parametric model

By letting the ground and volume structure matrices depend upon some physically meaningful parameter, equation (20) provides an easy access point to an effective modeling of the problem. In this chapter I will consider a very simple model, where both the ground and the vegetation layer are represented as phase centers plus the associated decorrelation term arising from the angular spreading described in section 2.4. Hence, the phase of the structure matrices can be parametrized as:

$$\angle \left\{ \mathbf{R}_{g,v} \right\}_{nm} = \frac{4\pi}{\lambda r} \frac{b_m - b_n}{\sin\theta} z_{g,v} \tag{21}$$

where $z_{g,v}$ is the elevation of the phase center associated with ground and volume scattering. As for the amplitudes, instead, the following model will be retained:

$$\left| \left\{ \mathbf{R}_{g,v} \right\}_{nm} \right| = \rho_{g,v}^{-|b_n - b_m|/\Delta_b} \tag{22}$$

where $\rho_{g,v}$ will be referred to as spreading constant and Δ_b is the average normal baseline sampling. The role of the spreading constant is to describe in a simple fashion the angular spreading that arises from the spatial structure associated to each phase center, avoiding the dependence upon a particular physical model. Given the definition above, the spreading constant ranges from 0 to 1, corresponding to the cases of pure noise and of a perfectly coherent received signal (i.e. a point-like scatterer), respectively. For details on more sophisticated physical models, the reader is referred to (13), (27).

3.3.1 Inversion

In principle, the availability of a model for the covariance matrix suffices for solving for the unknowns through Maximum Likelihood Estimation (MLE) (28). This solution, however, would not be efficient, since it requires an exhaustive search in a significantly wide parameter space. A significant complexity reduction may be achieved by applying the Covariance Matching Estimation Method (COMET) (29), (30), (31), (32), which allows to solve the problem by minimizing a weighted Frobenius norm of the difference between the sample covariance matrix and the model . In formula:

$$\left(\widehat{z}_g, \widehat{\rho}_g, \widehat{z}_g, \widehat{\rho}_g, \widehat{\sigma_g^2}, \widehat{\sigma_v^2} \right) = \text{argmin} \left\{ trace \left(\widehat{\mathbf{R}}^{-1} (\widehat{\mathbf{R}} - \mathbf{M}) \widehat{\mathbf{R}}^{-1} (\widehat{\mathbf{R}} - \mathbf{M}) \right) \right\} \tag{23}$$

where $\widehat{\mathbf{R}}$ is the sample covariance matrix and $\mathbf{M}$ is the model matrix, i.e.:

$$\mathbf{M} = \sigma_g^2 \mathbf{R}_g \left(z_g, \rho_g \right) + \sigma_v^2 \mathbf{R}_v \left(z_v, \rho_v \right). \tag{24}$$

A straightforward extension to the case of multi-polarimetric data can be achieved by assuming that backscattered powers $\left(\sigma_g^2, \sigma_v^2 \right)$ only change with polarization, whereas the structural parameters $\left(z_g, \rho_{g,} z_v, \rho_v \right)$ stay the same. See (26) for details.

3.4 A case study: the Remningstorp forest site

This section is devoted to reporting the results of the tomographic analysis of the forest site of Remningstorp, Sweden, on the basis of a data-set of $N = 9$ P-Band, fully polarimetric SAR images acquired by the DLR airborne system E-SAR in the frame of the ESA campaign BIOSAR 2007. Prevailing tree species in the imaged scene are Norway spruce (Picea abies), Scots pine (Pinus sylvestris) and birch (Betula spp.). The dominant soil type is till with a field layer, when present, of blueberry (Vaccinium myrtillus) and narrow thinned grass

(Deschampsia flexuosa). Tree heights are in the order of 20 m, with peaks up to 30 m. The topography is fairly flat, terrain elevation above sea level ranging between 120 and 145 m. The acquisitions have been carried out from March to May 2007. The horizontal baseline spacing is approximately 10 m, resulting in a maximum horizontal baseline of approximately 80 m. The spatial resolution is approximately 3 m in the slant range direction and 1 m in the azimuth direction. The look angle varies from 25° to 55° from near to far range, resulting in the vertical resolution to vary from about 10 m in near range to 40 m in far range. See also table (2) in the remainder.
The top row of Fig. (5) shows an optical view of the Remningstorp test site captured from Google Earth, re-sampled onto the SAR slant range, azimuth coordinates, whereas the bottom row of the same figure shows the amplitude of the HH channel, averaged over the 9 images. Backscatter from open areas has turned out to be remarkably lower than that from forested areas (about 25 dB), as expected at longer wavelengths.

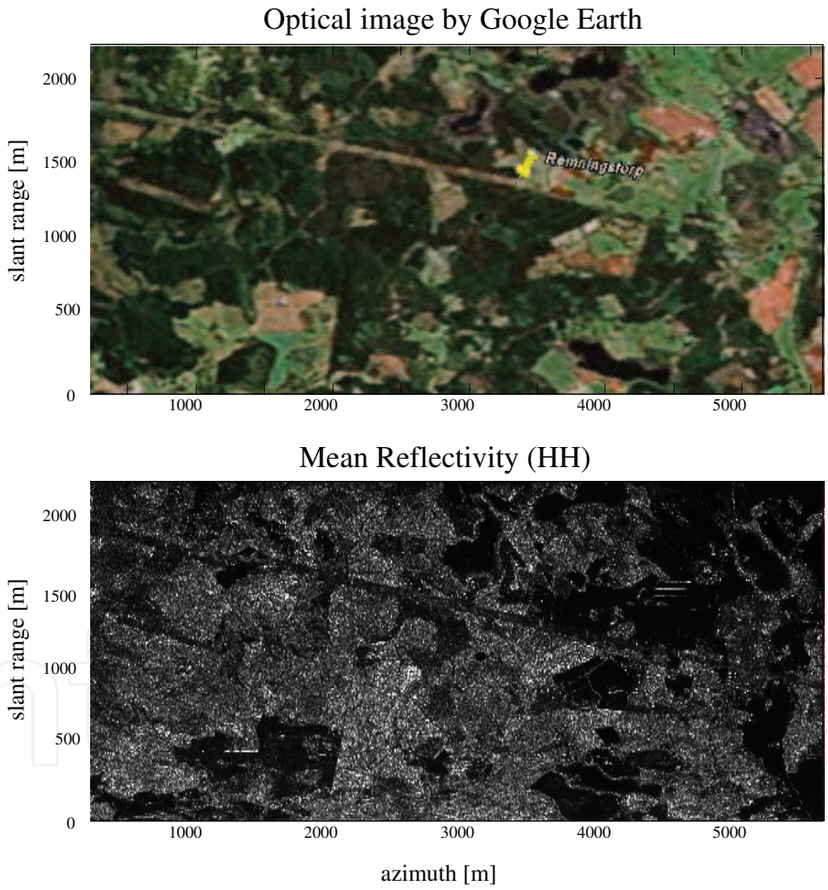

Fig. 5. Top row: Optical image of the Remningstorp forest site by Google Earth. Bottom row: Mean reflectivity of the HH channel.

3.4.1 Non tomographic analysis

An analysis of the amplitude stability of the data has been performed by computing the ratio μ/σ, where μ and σ denote the mean and the standard deviation of the amplitudes of the

SLC images. The μ/σ index is widely used in Permanent Scatterers Interferometry (PSI) as a criterion to select the most coherent scatterers in the imaged scene (33). As a result, for both the HH and VV channels the μ/σ index has resulted to be characterized by extremely high values ($\mu/\sigma > 15$), which indicates the presence of a highly stable scattering mechanism in the co-polar channels. Surprisingly, high values of the μ/σ index ($\mu/\sigma > 10$) have been observed in the HV channel as well.
Temporal decorrelation has been evaluated by exploiting the presence of additional zero baseline images. The temporal coherence at 56 days has been assessed in about $\gamma_{temp}^{HH} \simeq 0.85$ in the HH channel, $\gamma_{temp}^{VV} \simeq 0.8$ in the VV channel, and $\gamma_{temp}^{HV} \simeq 0.75$ in the HV channel, relatively to forested areas. Accordingly, the temporal stability of the scene is rather good for all the three polarimetric channels, indicating the presence of a stable scattering mechanism, especially in the co-polar channels.
The information carried by the co-polar channels has been analyzed by averaging the backscattered powers and the co-polar interferograms (i.e.: the Hermitian product between the HH and VV channels) over all the 9 tracks and inside an estimation window as large as 50×50 square meters (ground range, azimuth). The distribution of the HH and VV total backscattered power with respect to the co-polar phase, $\Delta\varphi = \varphi_{HH} - \varphi_{VV}$, has shown to be substantially bimodal, high and low energy values being concentrated around $\Delta\varphi \approx 80^\circ$ and $\Delta\varphi \approx 0^\circ$, respectively, see Fig.(6). The coherence between the HH and VV channels has been observed to be rather high in open areas ($\gamma_{copol} \approx 0.8$.), whereas in forested areas it has been assessed about $\gamma_{copol} \approx 0.45$.

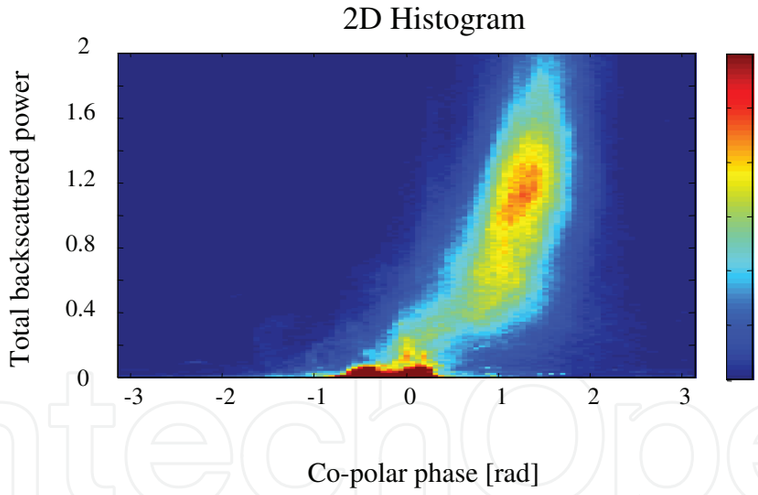

Fig. 6. Joint distribution of the total backscattered power and the co-polar phase for the co-polar channels. The total backscattered power has been obtained as the sum between the HH and VV backscattered powers. The color scale is proportional to the number of counts within each bin.

3.4.2 Tomographic analysis

A first, non parametric, tomographic analysis has been carried out by evaluating the Capon spectra of the three polarimetric channels, see for example (18), (17), reported in Fig. (7). Each spectrum has been obtained by evaluating the sample covariance matrix at each range bin on the basis of an estimation window as large as 50×50 square meters (ground range,

azimuth). The analyzed area corresponds to a stripe of the data along the slant range direction, shown in the top panel of Fig. (7). Almost the whole stripe is forested except for the dark areas in near range, corresponding to bare terrain. It may be observed that the three spectra have very similar characteristics. Each spectrum is characterized by a narrow peak, above which a weak sidelobe is visible. As for the co-polar channels, this result is consistent with the hypothesis that a single scattering mechanism is dominant. It is then reasonable to relate such scattering mechanism to the double bounce contribution from trunk-ground and canopy-ground interactions, and hence the peak of the spectrum can be assumed to be located at ground level. The sidelobe above the main peak is more evident in the HV channel, but the contributions from ground level seem to be dominant as well, the main peak being located almost at the same position as in the co-polar channels. Accordingly, the presence of a relevant contribution from the ground has to be included in the HV channel too.

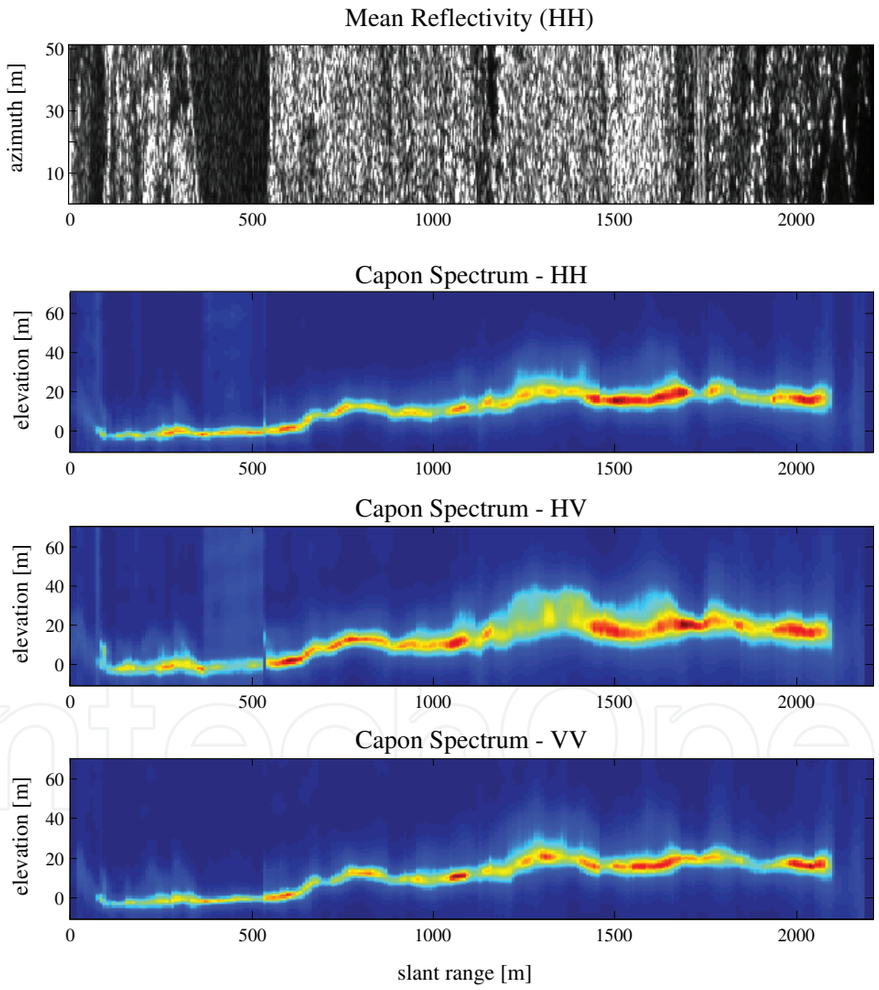

Fig. 7. Top panel: mean reflectivity of the data (HH channel) within a stripe as wide as 50 m in the azimuth direction. The underlying panels show the Capon Spectra for the three polarimetric channels. At every range bin the signal has been scaled in such a way as to have unitary energy.

3.4.3 Parametric tomographic analysis

Results shown here have been obtained by processing all polarizations at once, as suggested in section 3.3.1.

Figure (8) shows the map of the estimates relative ground elevation. The black areas correspond to absence of coherent signals, as it is the case of lakes. The estimates relative to canopy elevation are visible in Fig. (9). In this case, the black areas have been identified by the algorithm as being non-forested. It is worth noting the presence of a road, clearly visible in the optical image, see Fig. (5), crossing the scene along the direction from slant range, azimuth coordinates $(1850, 0)$ to $(1000, 5500)$. Along that road, a periodic series of small targets at an elevation of about 25 m has been found by the algorithm. Since a power line passes above the road, it seems reasonable to relate such targets to the echoes from the equipment on the top of the poles of the power line.

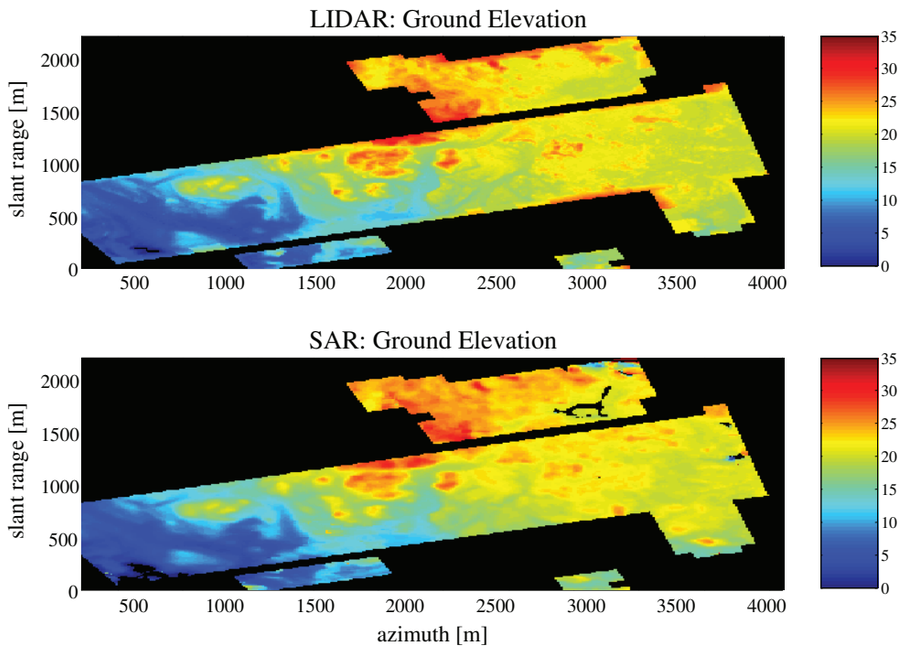

Fig. 8. Top row: ground elevation estimated by LIDAR. Bottom row: ground elevation estimated by T-SAR. Black areas correspond to an unstructured scattering mechanism.

As a validation tool, we used LIDAR measurements courtesy of the Swedish Defence Research Agency (FOI) and Hildur and Sven Wingquist's Foundation. Concerning ground elevation the dispersion of the difference $z_{SAR} - z_{LIDAR}$ has been assessed in less than 1 m. Concerning the estimated canopy elevation, the discrepancy with respect to LIDAR is clearly imputable to the fact that the estimates are relative to the average the *phase center* elevation inside the estimation window, whereas LIDAR is sensitive to the top height of the canopy. In particular, canopy elevation provided by T-SAR appears to be under-estimated with respect to LIDAR measurements, as a result of the under foliage penetration capabilities of P-band microwaves. Figure (10) reports the ratios between the estimated backscattered powers from the ground and the canopy (G/C ratio), for each polarimetric channel. As expected, in the co-polar channels the scattered power from the ground is significantly larger than canopy backscatter, the G/C ratio being assessed in about 10 dB. In the HV channel the backscattered powers

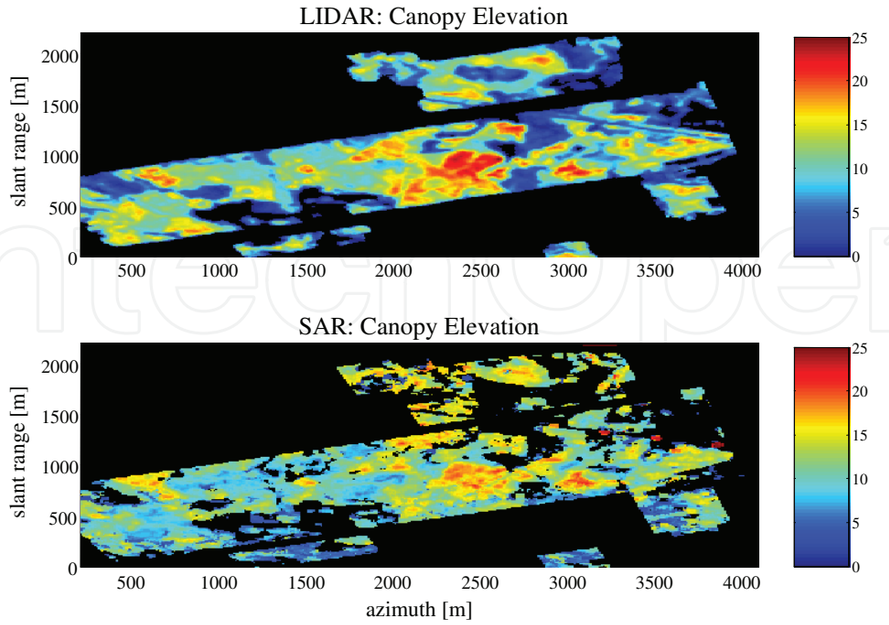

Fig. 9. Top row: canopy elevation estimated by LIDAR. Bottom row: canopy elevation estimated by T-SAR. Black areas correspond to absence of canopy.

from the ground and the canopy are closer to each other, even though ground contributions still appear to be dominant, resulting in a ground to canopy ratio of about 3 dB.

3.4.3.1 Single-polarization analysis

This last paragraph is dedicated to reporting the results relative to the elevation estimates provided by processing the HH, VV, and HV channel separately, compared to estimates yielded by the fully polarimetric (FP) tomography commented above. The joint distributions of the elevation estimates yielded by the FP tomography and by the single channel tomographies are reported in Fig. (11). It can be appreciated that, as expected, ground elevation is better estimated by processing the co-polar channel, whereas canopy elevation is better estimated by processing the HV channel. In all cases, however, the estimates are close to those provided by the FP tomography, proving that the tomographic characterization of forested areas may be carried out on the basis of a single polarimetric channel, provided that a sufficient number of acquisitions is available. It is important to note that the canopy phase center elevation yielded by the VV tomography has turned out to be slightly (between 1 and 2 meters) over estimated, with respect to both the FP tomography and to the HH and HV tomographies. This phenomenon indicates that the scatterers within the canopy volume exhibit a vertical orientation, as expected at longer wavelengths (34), (35). This result shows that effects of vegetation orientation at P-band are appreciable, and measurable by Tomography, but not so severe to hinder the applicability of the FP Tomography depicted above.

3.4.4 Discussion

Since the co-polar phase for both ground and canopy backscatter is expected to be null, (36), the value of $\Delta\varphi \approx 80^\circ$ found in forested areas can only be interpreted as an index of the

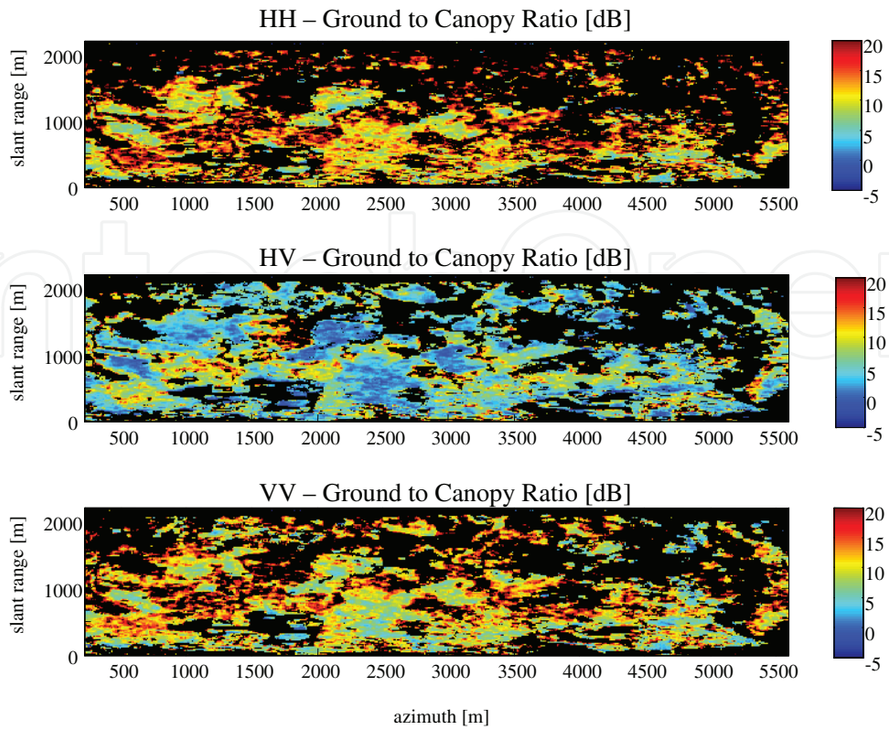

Fig. 10. Ground to Canopy Ratio for the three polarimetric channels.

presence of a dihedral contribution. Now, whereas for a perfect conducting dihedral $\Delta\varphi$ is exactly 180°, for a lossy dielectric dihedral a lower value of $\Delta\varphi$ is expected, due to the electromagnetic properties of the trunk-ground ensemble (in (37) for example, a co-polar phase of 94° has been observed for trunk-ground scattering). What makes the interpretation of the co-polar signature of forested areas not straightforward is that low values of the co-polar coherence have been observed, whereas dihedral contributions to the HH and VV channels are usually assumed to by highly correlated (36). A possible explanation would be to assume that forested areas are characterized by an almost ideal dihedral scattering plus a significant contribution from canopy backscatter, which would explain both the low co-polar coherence and the reduction of $\Delta\varphi$ from the ideal value of 180° to 80°. This interpretation, however, is not satisfying, since it is not consistent with the presence of highly amplitude stable targets nor with the Capon spectra in Fig. (7). At this point, a better explanation seems to be that to consider forested areas as being dominated by a *single* scattering mechanism, responsible for (most of) the coherence loss between the co-polar channels, highly coherent with respect to geometrical and temporal variations, and approximately located at ground level. From a physical point of view, it makes sense to relate such scattering mechanism to trunk-ground interactions, eventually perturbed by the presence of understory, trunk and ground roughness, small oscillations in the local topography, or eventually by canopy-ground interactions. Casting T-SAR as a parametric estimation problem has allowed to support such a conclusion by providing quantitative arguments such as the G/C ratios that indicate that not only in the co-polar channel, but also in the HV channel the contributions from the ground level dominate those from the canopy. Such result indicates that the ideal dihedral scattering model does not provide a sufficient description of the HV ground contributions under the forest, suggesting effects due to understory and volume-ground interactions.

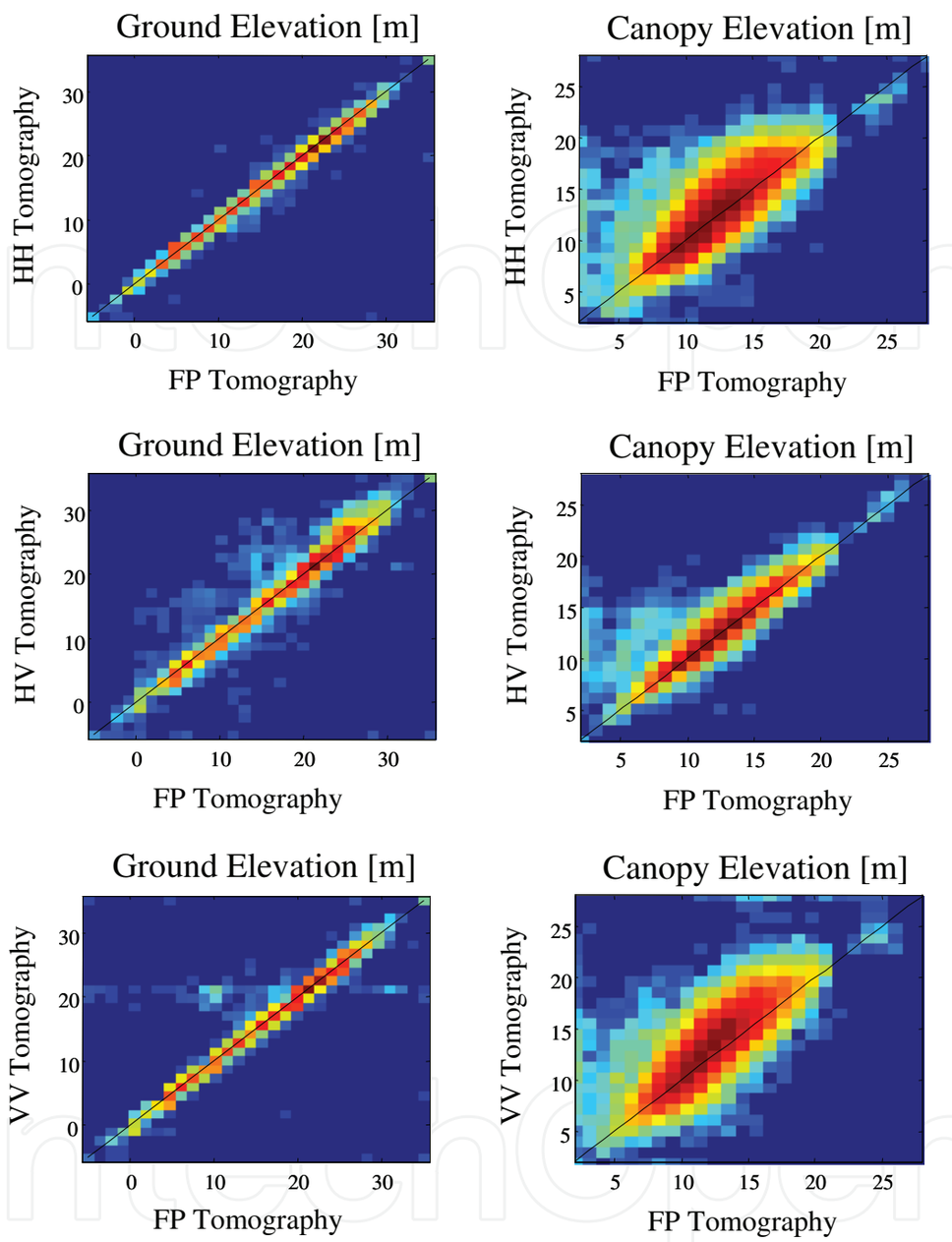

Fig. 11. Joint distribution of the phase center elevation estimates yielded by processing the single channels separately (vertical axis) and by the best tomography (horizontal axis). The black line denotes the ideal linear trend. The color scale is proportional to the natural logarithm of the number of counts within each bin.

4. Ground-volume decomposition from multi-baseline and multi-polarimetric data

4.1 Introduction

The idea that Radar scattering from forested areas can be well modeled as being constituted by two Scattering Mechanisms (SMs) has largely been retained in literature. In first place, the

assumption of two SMs matches the intuitive argument that a forested area is characterized by the presence of two objects, i.e.: the ground and the vegetation layer. This idea has been formalized in literature through different physical models, considering the features of ground and volume scattering in polarimetric data (38), single-polarization tomographic data, as shown in (26) and in the previous section, or in polarimetric and interferometric (PolInSAR) data (13), (39), (27). Beside physical soundness, however, the popularity of two-layered models is also due to the fact that they provide a sufficiently simple mathematical framework to allow model inversion. This is particularly important in PolInSAR analysis, where the assumption of two layers results in the coherence loci, namely the distribution of the interferometric coherence as a function of polarization, to be given by a straight line in the complex plane (39). This simple geometrical interpretation provides the key to decompose the interferometric coherence in ground-only and volume-only contributions, after which ground and volume parameters, like terrain topographic and canopy heights are retrieved. The analysis of the shape of the coherence loci also provides a direct idea about the soundness of approximating the scene as being constituted by two SMs, which allows to assess the impact of model mismatches (35). The Sum of Kronecker Product (SKP) structure has been proposed in (40) as a general framework to discuss problem inversion in both single and multi-baseline configurations, and independently on the particular physical model adopted to represent each SM. Concerning two-layered models, the SKP formalism leads to the conclusion that the correct identification of the structural and polarimetric properties of ground and volume scattering is subject to an ambiguity, in that different solutions exist that fit the data covariance matrix up to the same error. Such an ambiguity is shown to be completely described by two degrees of freedom, which can be resolved by employing physical models. In other words, the two dimensional ambiguity following after the SKP structure represents exactly the model space, meaning that a certain physical model corresponds to a certain solution of problem ambiguity, and vice-versa. Accordingly, the SKP formalism provides a way to discuss every possible physical model, by exploring the space of ambiguous solutions. In this chapter, this methodology is applied to data from the ESA campaigns BIOSAR 2007, BIOSAR 2008 and TROPISAR. Different models are being investigated by exploring different solutions in the ambiguous space, whose features are discussed basing on polarimetric and tomographic features.

4.2 The SKP structure

We consider a scenario where Radar scattering is contributed by multiple Scattering Mechanisms (SMs), as in forested areas, and assume a data-set of $N \cdot N_p$ SAR SLC images, N_p being the number of independent polarizations (typically $N_p = 3$) and N the number of passages over the scene. Let $y_n(\mathbf{w}_i)$ denote a complex-valued pixel of the image acquired from passage n in the polarization identified by the projection vector $\mathbf{w}_i$. A simple way to model the data second order statistics is to assume that: i) different SMs are uncorrelated with one another; ii) the correlation between any two passages, say n and m, of the *k-th* SM alone, $r_k(n,m)$, is invariant to polarization (up to a scale factor); iii) the correlation between any two polarizations, say $\mathbf{w}_i$ and $\mathbf{w}_j$, of each SM *alone*, $c_k\left(\mathbf{w}_i, \mathbf{w}_j\right)$, is invariant to the choice of the passage (up to a scale factor), see (40) for details. Under the three hypotheses above it follows that:

$$E\left[y_n(\mathbf{w}_i)\, y_m^*\left(\mathbf{w}_j\right)\right] = \sum_{k=1}^{K} c_k\left(\mathbf{w}_i, \mathbf{w}_j\right) r_k(n,m) \;\forall \mathbf{w}_i, \mathbf{w}_j, n, m \tag{25}$$

where K is the total number of SMs. Chosen an arbitrary polarization basis, we can recast (25) in matrix form as:

$$\mathbf{W} = \sum_{k=1}^{K} \mathbf{C}_k \otimes \mathbf{R}_k \tag{26}$$

where: $\otimes$ denotes Kronecker product; $\mathbf{W}$ ($\left[N \cdot N_p \times N \cdot N_p\right]$) is the covariance matrix of the multi-baseline and multi-polarimetric data; the matrices $\mathbf{C}_k$ ($\left[N_p \times N_p\right]$) and $\mathbf{R}_k$ ($[N \times N]$) are such that $c_k\left(\mathbf{w}_i, \mathbf{w}_j\right) = \mathbf{w}_i^H \mathbf{C}_k \mathbf{w}_j$ and $r_k(n,m) = \{\mathbf{R}_k\}_{nm}$ ($\{\}_{nm}$ denoting the $nm-th$ element of a matrix).

Accordingly, model (26) allows to represent each SM through a Kronecker product between two matrices. The first, $\mathbf{C}_k$, accounts for the correlation among different polarizations, and thus it represents the polarimetric properties of the $k-th$ SM, see for example (41). The second, $\mathbf{R}_k$, accounts for the correlation among different baselines, therefore carrying the information about the vertical structure of the $k-th$ SM [3]. The matrices $\mathbf{C}_k, \mathbf{R}_k$ will be hereinafter referred to as polarimetric signatures and structure matrices, respectively, by virtue of their physical meaning.

Following the arguments in (40), it can be shown that in most cases it can be assumed that the data covariance matrix is constituted by just two Kronecker Products, one associated with volume backscattering, and the other with the ensemble of all SMs whose phase center is ground locked, namely surface backscattering, ground-volume scattering, and ground-trunk scattering. Accordingly, eq. (26) defaults to:

$$\mathbf{W} = \mathbf{C}_g \otimes \mathbf{R}_g + \mathbf{C}_v \otimes \mathbf{R}_v \tag{27}$$

where the subscript v refers to volume backscattering and the subscript g refers to all SMs whose phase center is ground locked. For sake of simplicity, hereinafter we will refer to the two terms in (27) simply as ground scattering and volume scattering. It is worth noting that the assumption of two Kronecker Products can be approximately retained also in the case of an Oriented Volume over Ground (OVoG), by interpreting the matrix $\mathbf{R}_v$ as the average volume structure matrix across all polarizations (40).

4.3 Model representation

The key to the exploitation of the SKP structure is the important result, due to Van Loan and Pitsianis (42), after which *every* matrix can be decomposed into a SKP. It is shown in (40) that the terms of the SKP Decomposition are related to the matrices $\mathbf{C}_k, \mathbf{R}_k$ via a linear, invertible transformation, which is defined by exactly $K(K-1)$ real numbers. Assuming $K = 2$ SMs, as in the case of ground and volume scattering, it follows that there exist 2 real numbers (a, b)

[3] Neglecting temporal decorrelation and assuming target stationarity, the $nm-th$ entry of the matrix $\mathbf{R_k}$ is obtained as (18), (6), (26):

$$\{\mathbf{R}_k\}_{nm} = \int S_k(z)\, exp\left\{j\left(k_z(n) - k_z(m)\right) z\right\} dz$$

where z is the vertical coordinate, $S_k(z)$ is the vertical profile of the backscattered power for the $k-th$ SM, $k_z(n)$ is the height to phase conversion factor for the $n-th$ image (7). It is worth noting that eventual temporal coherence losses would be completely absorbed by the matrices $\mathbf{R}_k$, as discussed in (40). Accordingly, in presence of temporal decorrelation nothing changes as for the validity of model (26), but it should be kept in mind that in this case the matrices $\mathbf{R}_k$ would represent not only the spatial structure, but also the temporal behavior of the $k-th$ SM.

such that:

$$\begin{aligned}
\mathbf{R}_g &= a\widetilde{\mathbf{R}}_1 + (1-a)\,\widetilde{\mathbf{R}}_2 \\
\mathbf{R}_v &= b\widetilde{\mathbf{R}}_1 + (1-b)\,\widetilde{\mathbf{R}}_2 \\
\mathbf{C}_g &= \frac{1}{a-b}\left((1-b)\,\widetilde{\mathbf{C}}_1 - b\widetilde{\mathbf{C}}_2\right) \\
\mathbf{C}_v &= \frac{1}{a-b}\left(-(1-a)\,\widetilde{\mathbf{C}}_1 + a\widetilde{\mathbf{C}}_2\right)
\end{aligned} \tag{28}$$

where $\widetilde{\mathbf{R}}_k, \widetilde{\mathbf{C}}_k$ are two sets of matrices yielded by the SKP Decomposition, see (40).
It is very important to point out that the choice of the parameters (a, b) in (28) does affect the solution concerning the retrieval of the polarimetric signatures and structure matrices for ground and volume scattering, whereas the sum of their Kronecker products is invariant to choice of (a, b). In other words, the SKP Decomposition yields two sets of matrices that can be linearly combined so as to reconstruct exactly the structure matrices and polarimetric signatures associated with ground and volume scattering. Yet, the coefficients of such a linear combination are not known. An obvious criterion to eliminate non-physically valid solutions is to admit only values of (a, b) that yield, through (28), (semi)positive definite polarimetric signatures and structure matrices for both ground and volume scattering. We will define the set of values of (a, b) corresponding to physically valid solutions as Region of Physical Validity (RPV). Details about the RPV are provided in the remainder.
Suppose now that a certain matrix W_{mod} is the best estimate of the true data covariance matrix in a certain metric, and also suppose that $\mathbf{W}_{mod}$ can be written as the sum of 2 KPs. What equations (28) state is that there exist infinite ways of representing the matrix W_{mod}, each of which corresponding to a particular value of the parameters (a, b). The parameters (a, b) then represents the ambiguity of the ground-volume decomposition problem, meaning that by varying (a, b) within the RPV we end up with different physically valid polarimetric signatures and structure matrices, yet entailing no variations of the degree of fitness of W_{mod} with respect to the original data. In other words, each *solution* of the ambiguity associated with the choice of (a, b) within the RPV represents a particular *physically valid and data-consistent model* for both the polarimetric signatures and the structure matrices of ground and volume scattering.

4.4 Regions of Physical Validity (RPV)

In this section we discuss the shape of the RPV, under the assumption that the data covariance matrix is actually a sum of $K = 2$ KPs representing ground and volume scattering, according to model (27).
An exact procedure for the determination of the RPV has been derived in (40), by recasting equation (28) in diagonal form. Although the procedure is straightforward, its description involves quite lengthy matrix manipulations. For this reason, we will discuss here the shape of the RPV by resorting to a useful geometrical interpretation. To do this we will assume the Polarimetric Stationarity Condition to hold (43), resulting in the structure matrix of each SM to have unitary elements on the main diagonal, see(40). This property is inherited by the matrices $\widetilde{\mathbf{R}}_1$,$\widetilde{\mathbf{R}}_2$ in (28), which allows to interpret the off diagonal elements of $\mathbf{R}_g$,$\mathbf{R}_v$ as the complex interferometric coherence of ground and volume scattering (the elements on their diagonal being identically equal to 1). It is then immediate to see from equation (28) that, in each interferogram, ground and volume coherences are bound to lie on a straight line in the complex plane. Accordingly, the optimal choice of the parameters (a, b) is the

Branch	Boundary	Rank-deficient matrix
a	Inner	$\mathbf{C}_v$
a	Outer	$\mathbf{R}_g$
b	Inner	$\mathbf{C}_g$
b	Outer	$\mathbf{R}_v$

(29)

Table 1. Rank deficiencies at the boundaries of the region of positive definitiveness.

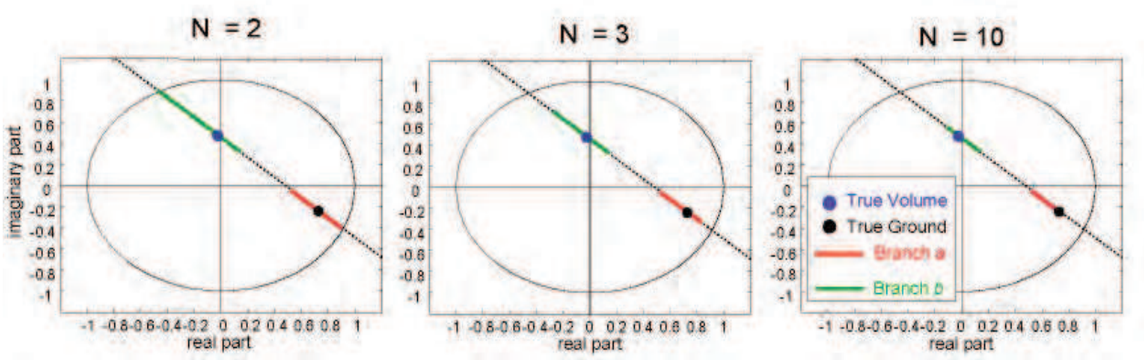

Fig. 12. Regions of physical validity for the interferometric coherences associated with ground and volume scattering in the interferometric pair between the first two tracks of the data-set. N is the total number of available tracks exploited to enforce the positive definitiveness constraint. The black and blue points denote the true interferometric coherences associated with ground and volume scattering in the considered interferometric pair. The red and green segments denote the set of all physically valid solutions obtained by varying a and b, respectively.

one that corresponds to the true[4] ground and volume coherences, whereas the region of physical validity can be simply associated with two segments along the line passing through the true ground and volume coherences, see figure 12. By definition, the points outer or inner boundaries of the two segments correspond to the case where one of the four matrices $\{\mathbf{C}_k, \mathbf{R}_k\}_{k=g,v}$ in equations (28) is singular. In particular, the outer boundaries correspond to rank-deficient structure matrices, whereas the inner boundaries correspond to rank-deficient polarimetric signature, as reported in Table 1. In the single baseline case ($N = 2$) the points at the outer boundary of both segments belong to the unit circle, indicating that physically valid ground and volume interferometric coherences are allowed be unitary in magnitude, see figure 12, left panel. This conclusion is exactly the same as the one drawn in (39), after which it follows the consistency of the SKP formalism with respect to PolInSAR. As new acquisitions are gathered, instead, the positive definitiveness constraint results in the regions of physical validity to shrink from the outer boundaries towards the true ground and volume coherences, whereas the position of the inner boundary points stay unvaried for the considered interferogram, figure 12, middle and right panels. Accordingly, the availability of multiple-baseline results not only in enhanced vertical resolution capabilities, but also in the progressive elimination of incorrect solutions.

[4] Assuming (27).

Campaign	BioSAR 2007
Acquisition System	E-SAR - DLR
Acquisition Period	Spring 2007
Site	Remningstorp, Central Sweden
Scene	Semi-boreal forest
Topography	Flat
Tomographic Tracks	9 - Fully Polarimetric
Band	P-Band
Slant Range resolution	2 m
Azimuth resolution	1.6 m
Vertical resolution	10 m (near range) to 40 m (far range)

Table 2. The BIOSAR 2007 data-set

4.5 Physical interpretation

A straightforward physical interpretation of the polarimetric and structural properties of models associated with different solutions can be provided by analyzing the inner and outer boundaries of the RPV:

- The inner boundary solution on branch *a* results in the volume polarimetric signature to be rank-deficient. This entails the existence of a polarization where volume scattering does not contribute, after which it follows that this solution is not consistent with physical model for forest scattering (44), (38). The ground structure matrix is characterized by the lowest coherence values, being contaminated by volume contributions. Accordingly, such a solution is to be discarded.
- The outer boundary solution on branch *a* results in the volume polarimetric signature to be full rank, consistently with physical model for forest scattering. The resulting ground structure matrix is characterized by the highest coherence values compatible with the RPV. Provided the number of tracks is sufficient, this solution yields an unbiased estimation of the ground coherences even in presence of coherence losses.
- The inner boundary solution on branch *b* results in the ground polarimetric signature to be rank-deficient, consistently with the hypothesis that there exists one polarization where volume only contributions are present. If this is true, the resulting volume structure corresponds to the true one. Otherwise, the result is systematically contaminated by ground contributions, resulting in apparent volume contributions close to the ground.
- The outer boundary solution on branch *b* results in the ground polarimetric signature to be full rank. Accordingly, this solution accounts for the presence of ground-locked contributions in all polarizations. The resulting volume structure matrix is maximally coherent. If few tracks are employed, this solution acts as an high-pass filter, resulting in the volume to appear thinner than it is. As the number of available baselines increases, this solution converges to the true structure for volume contributions in the upper vegetation layers, whereas volume contributions from the ground level are absorbed into the ground structure.

4.6 Case studies

We present here experimental results relative to three case studies based on data from the ESA campaigns BIOSAR 2007 (45), BIOSAR 2008 (46) and TROPISAR. The main features of the analyzed data are reported in tables 2, 3, 4.

Campaign	BioSAR 2008
Acquisition System	E-SAR - DLR
Acquisition Period	Fall 2008
Site	Krycklan river catchment, Northern Sweden
Scene	Boreal forest
Topography	Hilly
Tomographic Tracks	6 per flight direction (South-West and North-East) – Fully Polarimetric
Band	P-Band and L-Band
Slant Range resolution	1.5 m
Azimuth resolution at L-Band	1.2 m
Azimuth resolution at P-Band	1.6 m
Vertical resolution at L-Band	6 m (near range) to 40 m (far range)
Vertical resolution at P-Band	20 m (near range) to >80 m (far range)

Table 3. The BioSAR 2008 data-set

Campaign	TropiSAR
Acquisition System	Sethi- ONERA
Acquisition Period	August 2009
Site	Paracou, French Guyana
Scene	Tropical forest
Topography	Flat
Tomographic Tracks	6 - Fully Polarimetric
Band	P-Band
Slant Range resolution	1 m
Azimuth resolution	1 m
Vertical resolution	$\simeq$15 m

Table 4. The TropiSAR data-set

All of the result to follow have been obtained by estimating the sample covariance matrix of the multi-baseline and multi-polarimetric data by multi-looking over a 60×60 m (ground range, azimuth) estimation window.

4.6.1 Models for the volume structure

Figures from13 to 16 report tomographic images of the volume structures as obtained by taking three different solutions on branch b. The tomographic imaging has been performed by employing the Capon Spectral Estimator.

All the tomographic profiles behave consistently with the physical features discussed in the previous section. In particular, all profiles associated with the outer boundary solution result in very thin volumes at a high elevation, therefore accounting for the upper vegetation layer only. As the solution is moved towards the inner boundary contributions from the lower vegetation layer appear. When the inner boundary is reached the the contributions appear from the ground level up to top forest height. The following points are worth noting:

- Contributions from the ground level are observed in all cases in the inner boundary solution. As this solution corresponds by construction to the polarization where ground

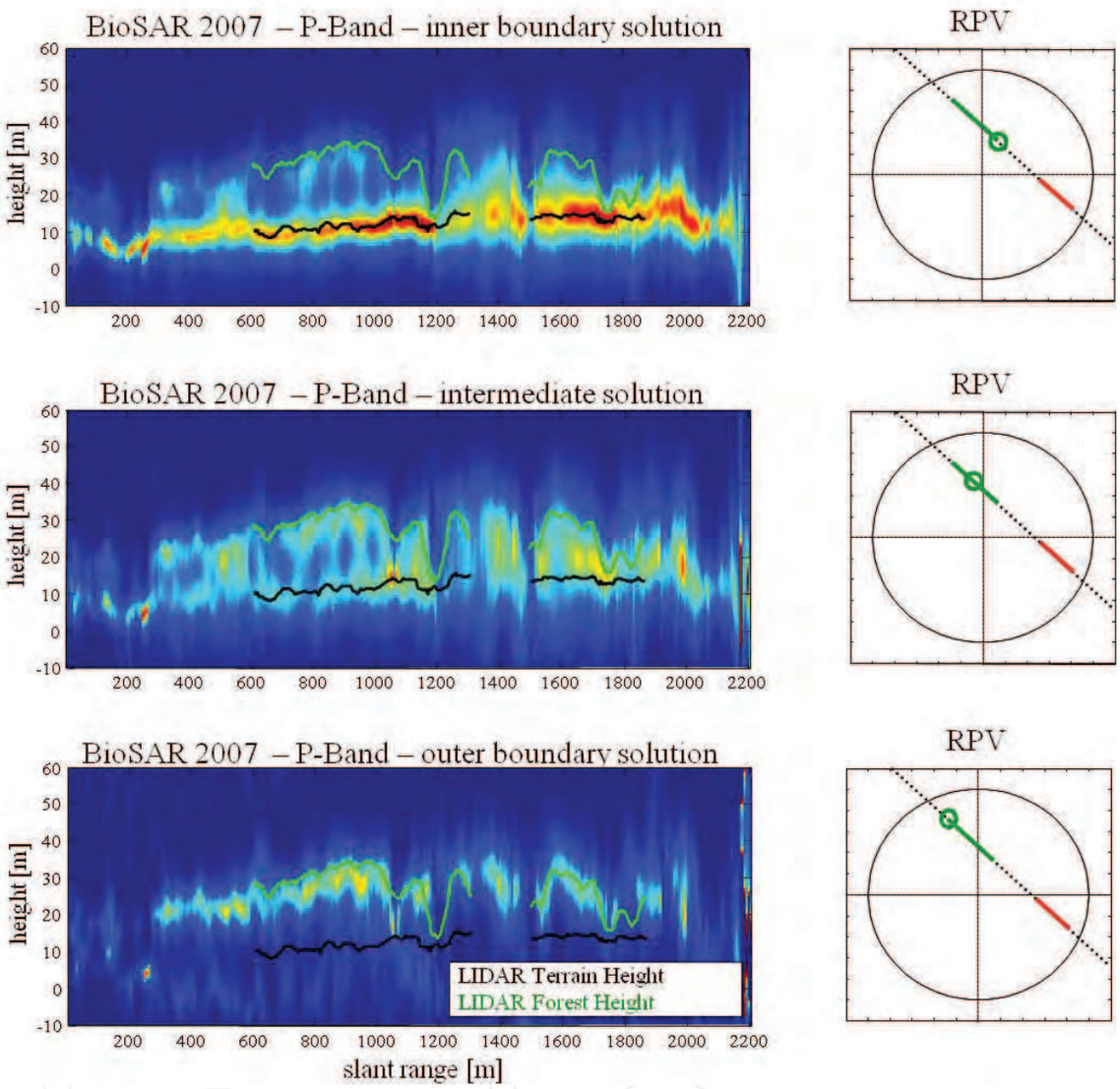

Fig. 13. Tomographic profiles along an azimuth cut corresponding to three different physically valid models for the volume structure.

scattering is not supposed to occur, we conclude that depolarized contributions from the ground level are present in all data-sets. The extent of such contributions is by far more relevant in the case of the BioSAR 2007 and BioSAR 2008 P-Band data-sets, witnessing the sensitivity of the data to both wavelength and forest structure.

- The position along the vertical axis at which the backscattered power drops down is independent of the choice of the solution, meaning that all solutions carry the same information about forest top height.

4.6.2 Fitness

The figure below reports the amount of information carried by the data that is correctly represented by assuming the data covariance matrix is a sum of 1 to 4 KPs. The measurement

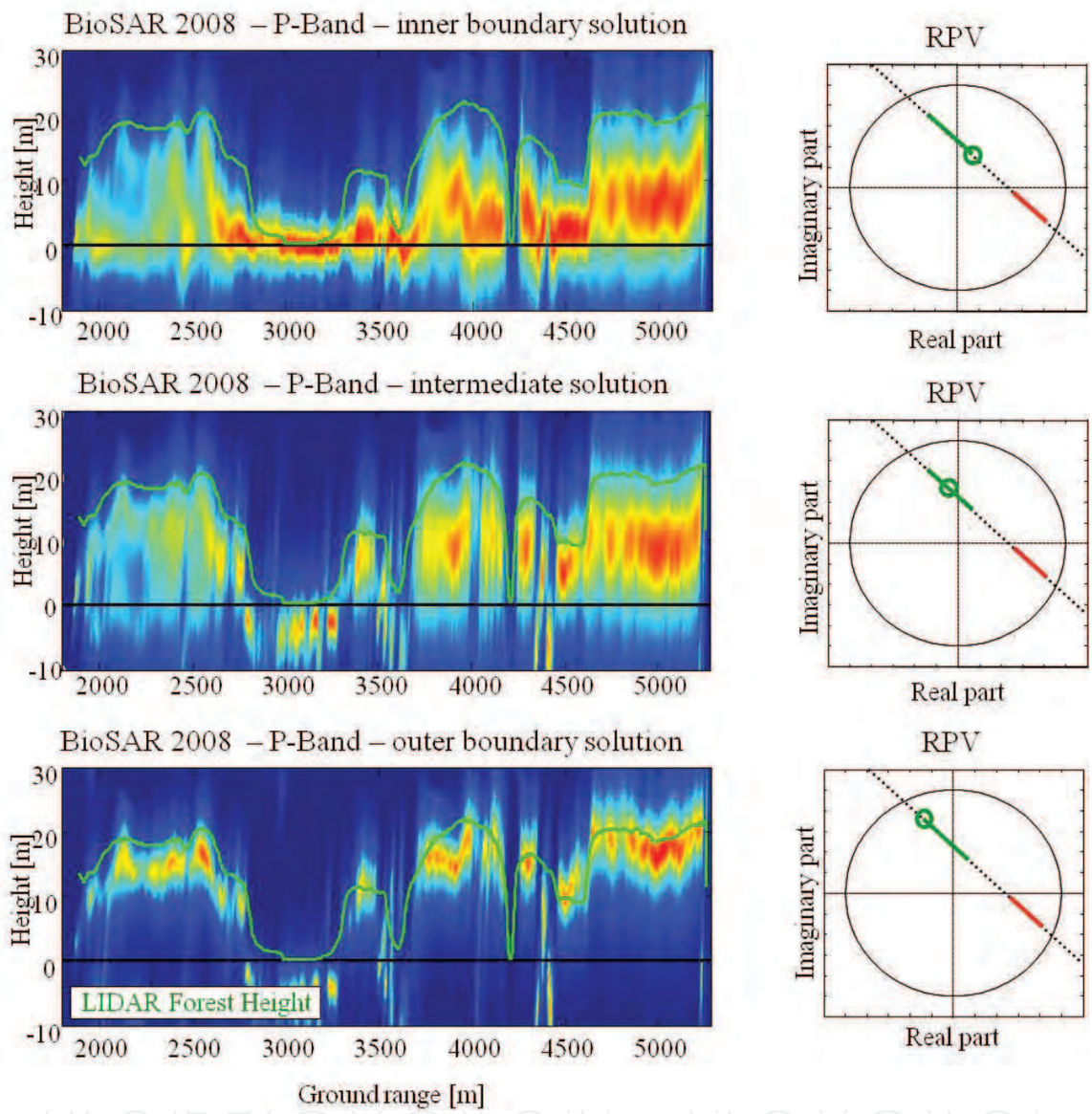

Fig. 14. Tomographic profiles along an azimuth cut corresponding to three different physically valid models for the volume structure. Note that topography has been removed such that the ground level is always at 0 m.

is carried out as $I_K = 1 - \varepsilon_K$, ε_K being defined as:

$$\varepsilon_K = \frac{\left\| \widehat{\mathbf{W}} - \widehat{\mathbf{W}}_K \right\|_F}{\left\| \widehat{\mathbf{W}} \right\|_F}$$

where $\widehat{\mathbf{W}}$ is the sample covariance matrix and $\widehat{\mathbf{W}}_K$ its best estimate in the Frobenius norm by using K KPs, see (40) for details.

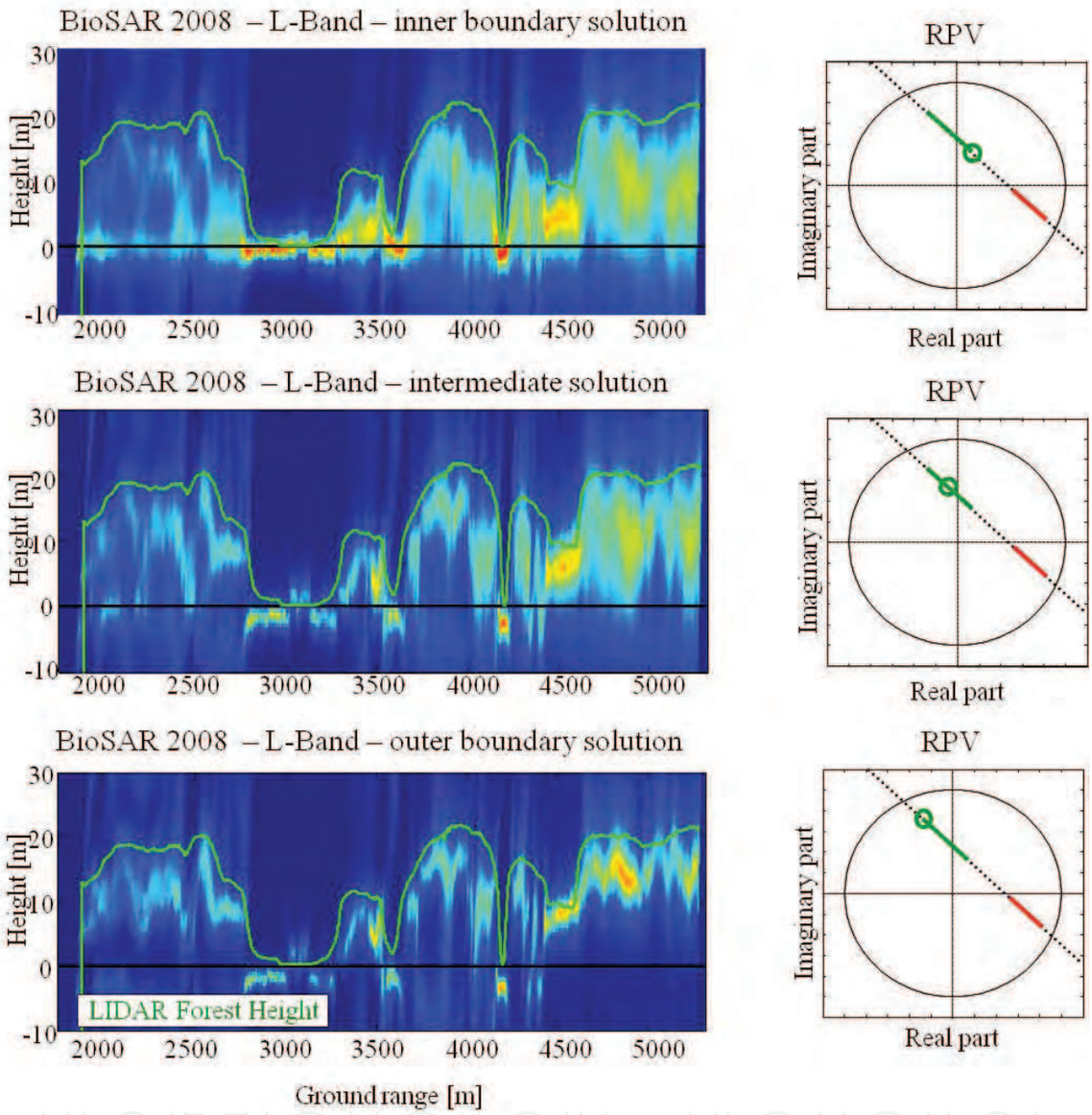

Fig. 15. Tomographic profiles along an azimuth cut corresponding to three different physically valid models for the volume structure. Note that topography has been removed such that the ground level is always at 0 m.

4.7 Discussion

On the basis of the analyzed data-sets, the following conclusions are drawn:

- The assumption of 2 KPs has turned out to account for about 90% of the information carried by the data in all investigated cases, meaning that two-layered models (ground plus volume) are well suited for forestry investigations. Accounting for other components, such as subsurface penetration or differential extinction phenomena, does not appear to be necessary as for a first-order characterization of the forest structure, their role being limited to about 10% of the total information content.

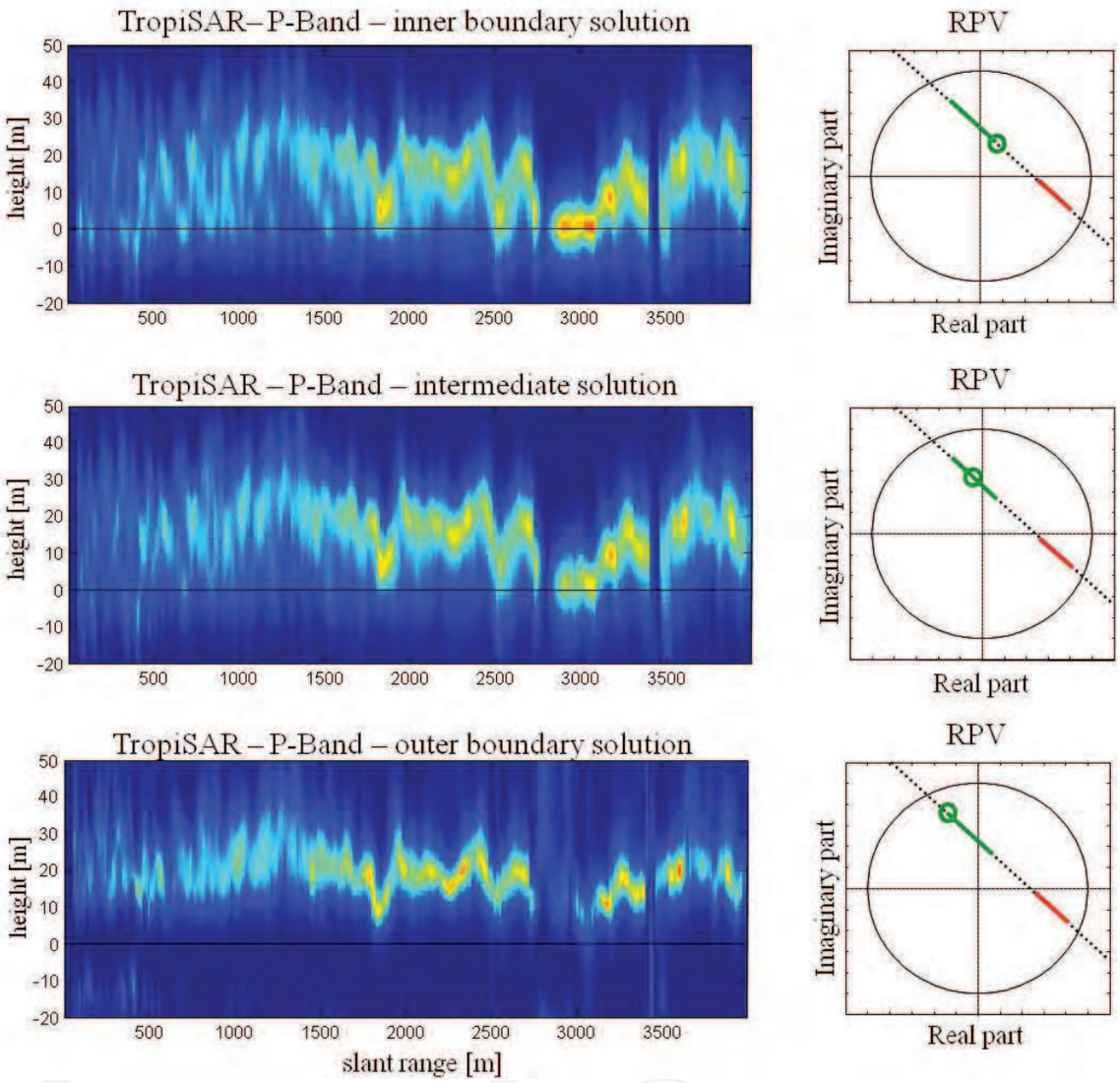

Fig. 16. Tomographic profiles along an azimuth cut corresponding to three different physically valid models for the volume structure. Note that topography has been removed such that the ground level is always at 0 m.

- The assumption of a ground-free polarization has resulted in an evenly distributed volume structure in a boreal forest at L-Band and in a tropical forest at P-Band, and in an almost ground-locked volume structure in a boreal and semi-boreal forest at P-Band, witnessing the sensitivity of Radar data to wavelength and forest structure. The extent of depolarized contributions from the ground level suggests ground-volume interaction phenomena may occur at P-Band in sparse forests. If this is the case, volume backscattering can be retrieved by allowing ground scattering to be partly entropic.
- The retrieval of forest top height is nearly invariant to the choice of the model. In this sense, forest top height appears as the most robust indicator of the forest structure as observed through microwaves measurements, providing a further and independent argument supporting the validity of PolInSAR for the remote sensing of forested scenarios.

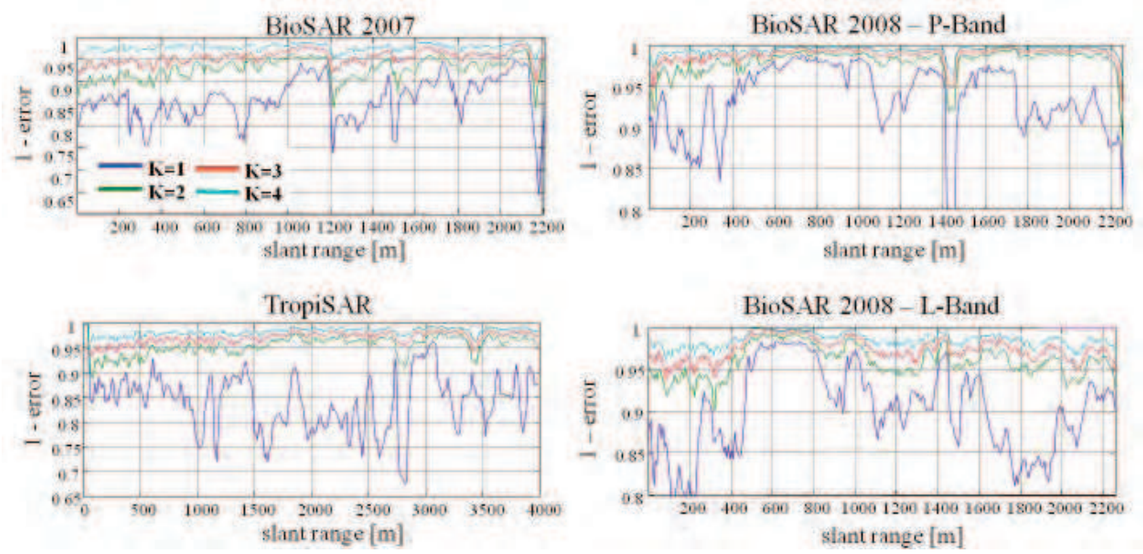

Fig. 17. Information content represented by taking K KPs for the four analyzed data-sets.

On the other hand, though, retrieving the correct forest height does not provide arguments to assess the validity of the whole model, as the same top height is consistent with different physically valid data-consistent models.

5. Conclusions

This chapter has considered the retrieval of information about the forest vertical structure from multi-baseline SARs.

Considering a purely tomographic formulation of the problem, it has been shown that the backscattered power associated with a certain depth within the vegetation layer can be retrieved with a *virtually* arbitrary resolution, simply by employing a sufficiently large baseline apertures. Besides costs, however, baseline aperture is upper bounded by physical constraints arising from the nature of the targets themselves, such as anisotropy and temporal decorrelation.

Posing T-SAR as an estimation problems greatly helps compensate for the coarse resolution arising from an insufficient baseline aperture, allowing to retrieve useful information about the forest structure even in cases where the Fourier resolution is many times the overall forest height. In particular, T-SAR has been shown to be capable of identifying bald and forested areas and estimating the elevation and backscattered power of the scattering centers representing associated with ground and volume scattering. Furthermore, it has been shown that T-SAR can be employed basing on both single and multi-polarimetric data, which makes T-SAR a valuable tool to investigate variations of the forest structure with polarization.

The availability of multi-polarimetric and multi-baseline data has been shown to provide the most information, allowing the decomposition of the data covariance matrix into ground-only and volume-only contributions even in absence of a parametric model and largely independently on baseline aperture.

The capability of the SKP formalism to represent *all* physically valid and data-consistent two-layered models has allowed an exhaustive discussion about the validity of such a class of models for the analysis of forested areas. As a result, it has been observed that two SMs account for more than 90% of the information carried by the data in all investigated cases.

The correct identification of physical models for such two SMs has been shown to be subject to an ambiguity, mostly associated with the possibility that depolarized contributions occur at the ground level as well. Furthermore, the correct retrieval of volume top height has been shown not to constitute a meaningful tool for model validation, being substantially invariant to the choice of the solution for volume scattering. In this framework it is then clear that tomographic imaging represents a most valuable tools for the assesment of physical models of the forest structure, as it allows to *see* what kind of vertical structure is actually associated with the chosen model.

6. Acknowledgment

I wish to acknowledge insights and valuable discussions with Prof. Fabio Rocca, Prof. Andrea Monti Guarnieri, and eng. Mauro Mariotti d'Alessandro at Politecnico di Milano. I also wish to thank to Dr. Malcom Davidson (ESA), Dr. Irena Hajnsek (DLR), Dr. Kostas Papathanassiou (DLR), Dr. Fabrizio Lombardini (Universitè di Pisa), Prof. Lars Ulander (FOI), Dr. Pascale Dubois-Fernandez (ONERA), Dr. Thuy Le Toan (CESBIO) with whom I have discussed many of the results within this chapter.

7. References

[1] J. C. Curlander and R. N. McDonough, *Synthetic aperture radar: systems and signal processing*. New York: John Wiley & Sons, Inc, 1991.

[2] G. Franceschetti and R. Lanari, Eds., *Synthetic Aperture Radar processing*. CRC Press, 1999.

[3] F. Rocca, "Synthetic aperture radar: A new application for wave equation techniques," *Stanford Exploration Project Report*, vol. SEP-56, pp. 167–189, 1987.

[4] R. Bamler, "A comparison of range-Doppler and wave-number domain SAR focusing algorithms," *IEEE Transactions on Geoscience and Remote Sensing*, vol. 30, no. 4, pp. 706–713, Jul. 1992.

[5] R.-S. Wu and M.-N. Toksï¿œz, "Diffraction tomography and multisource holography applied to seismic imaging," *Geophysics*, vol. 52, pp. 11–+, Jan. 1987.

[6] A. Reigber and A. Moreira, "First demonstration of airborne SAR tomography using multibaseline l-band data," *IEEE Trans. on Geoscience and Remote Sensing*, pp. 2142–2152, Sep. 2000.

[7] R. Bamler and P. Hartl, "Synthetic aperture radar interferometry," *Inverse Problems*, vol. 14, pp. R1–R54, 1998.

[8] F. Ulaby, K. McDonald, K. Sarabandi, and M. Dobson, "Michigan microwave canopy scattering models (mimics)," *Geoscience and Remote Sensing Symposium, 1988. IGARSS '88. Remote Sensing: Moving Toward the 21st Century., International*, vol. 2, pp. 1009–1009, Sep 1988.

[9] G. Smith-Jonforsen, L. Ulander, and X. Luo, "Low vhf-band backscatter from coniferous forests on sloping terrain," *Geoscience and Remote Sensing, IEEE Transactions on*, vol. 43, no. 10, pp. 2246–2260, Oct. 2005.

[10] L. Thirion, E. Colin, and C. Dahon, "Capabilities of a forest coherent scattering model applied to radiometry, interferometry, and polarimetry at p- and l-band," *Geoscience and Remote Sensing, IEEE Transactions on*, vol. 44, no. 4, pp. 849–862, April 2006.

[11] Y.-C. Lin and K. Sarabandi, "Electromagnetic scattering model for a tree trunk above a tilted ground plane," *Geoscience and Remote Sensing, IEEE Transactions on*, vol. 33, no. 4, pp. 1063–1070, Jul 1995.

[12] K. Sarabandi, "Scattering from dielectric structures above impedance surfaces and resistive sheets," *Antennas and Propagation, IEEE Transactions on*, vol. 40, no. 1, pp. 67–78, Jan 1992.
[13] R.N. Treuhaft, P.R. Siqueira, "Vertical structure of vegetated land surfaces from interferometric and polarimetric radar," *Radio Science*, vol. 35, pp. 141–177, 2000.
[14] P. Stoica and R. L. Moses, *Introduction to Spectral Analysis*. New Jersey: Prentice-Hall, 1997.
[15] H. A. Zebker and J. Villasenor, "Decorrelation in interferometric radar echoes," *IEEE Transactions on Geoscience and Remote Sensing*, vol. 30, no. 5, pp. 950–959, sept 1992.
[16] I. Hajnsek, F. Kugler, S.-K. Lee, and K. Papathanassiou, "Tropical-forest-parameter estimation by means of pol-insar: The indrex-ii campaign," *Geoscience and Remote Sensing, IEEE Transactions on*, vol. 47, no. 2, pp. 481 –493, feb. 2009.
[17] F. Lombardini and A. Reigber, "Adaptive spectral estimation for multibaseline SAR tomography with airborne l-band data," *Geoscience and Remote Sensing Symposium, 2003. IGARSS '03. Proceedings. 2003 IEEE International*, vol. 3, pp. 2014–2016, July 2003.
[18] F. Gini, F. Lombardini, and M. Montanari, "Layover solution in multibaseline SAR interferometry," *Aerospace and Electronic Systems, IEEE Transactions on*, vol. 38, no. 4, pp. 1344–1356, Oct 2002.
[19] S. Sauer, L. Ferro-Famil, A. Reigber, and E. Pottier, "Multibaseline pol-insar analysis of urban scenes for 3d modeling and physical feature retrieval at l-band," *Geoscience and Remote Sensing Symposium, 2007. IGARSS 2007. IEEE International*, pp. 1098–1101, 23-28 July 2007.
[20] X. X. Zhu and R. Bamler, "Very high resolution spaceborne sar tomography in urban environment," *Geoscience and Remote Sensing, IEEE Transactions on*, no. 99, pp. 1–13, 2010.
[21] G. Fornaro and F. Serafino, "Imaging of single and double scatterers in urban areas via SAR tomography," *Geoscience and Remote Sensing, IEEE Transactions on*, vol. 44, no. 12, pp. 3497–3505, Dec. 2006.
[22] G. Fornaro, F. Lombardini, and F. Serafino, "Three-dimensional multipass SAR focusing: experiments with long-term spaceborne data," *Geoscience and Remote Sensing, IEEE Transactions on*, vol. 43, no. 4, pp. 702–714, April 2005.
[23] S. R. Cloude, "Dual-baseline coherence tomography," *Geoscience and Remote Sensing Letters, IEEE*, vol. 4, no. 1, pp. 127–131, Jan. 2007.
[24] ——, "Multifrequency 3d imaging of tropical forest using polarization coherence tomography," in *Eusar 2008*, 2008.
[25] K. Papathanassiou and S. Cloude, "Single-baseline polarimetric SAR interferometry," *Geoscience and Remote Sensing, IEEE Transactions on*, vol. 39, no. 11, pp. 2352–2363, Nov 2001.
[26] S. Tebaldini, "Single and multipolarimetric SAR tomography of forested areas: A parametric approach," *Geoscience and Remote Sensing, IEEE Transactions on*, vol. 48, no. 5, pp. 2375 –2387, may 2010.
[27] M. Neumann, L. Ferro-Famil, and A. Reigber, "Estimation of forest structure, ground, and canopy layer characteristics from multibaseline polarimetric interferometric sar data," *Geoscience and Remote Sensing, IEEE Transactions on*, vol. 48, no. 3, pp. 1086 –1104, 2010.
[28] H. V. Trees, *Detection, Estimation and Modulation Theory, Part I*. New York, NY: John Wiley and Sons, 1968.
[29] P. Stoica and T. Soderstrom, "On reparametrization of loss functions used in estimation and the invariance principle," *Signal Processing*, no. 17, pp. 383–387, 1989.

[30] A. Swindlehurst and P. Stoica, "Maximum likelihood methods in radar array signal processing," *Proceedings of the IEEE*, vol. 86, no. 2, pp. 421–441, Feb 1998.
[31] P. S. B. Ottersten and R. Roy, "Covariance matching estimation techniques for array signal processing applications," *Digital Signal Processing*, no. 8(3), pp. 185–210, 1998.
[32] B. Jansson, M.; Ottersten, "Structured covariance matrix estimation: a parametric approach," *Acoustics, Speech, and Signal Processing, 2000. ICASSP '00. Proceedings. 2000 IEEE International Conference on*, vol. 5, pp. 3172–3175 vol.5, 2000.
[33] A. Ferretti, C. Prati, and F. Rocca, "Permanent scatterers in SAR interferometry," *IEEE Transactions on Geoscience and Remote Sensing*, vol. 39, no. 1, pp. 8–20, Jan. 2001.
[34] R. Treuhaft and S. Cloude, "The structure of oriented vegetation from polarimetric interferometry," *Geoscience and Remote Sensing, IEEE Transactions on*, vol. 37, no. 5, pp. 2620–2624, Sep 1999.
[35] J. Lopez-Sanchez, J. Ballester-Berman, and Y. Marquez-Moreno, "Model limitations and parameter-estimation methods for agricultural applications of polarimetric SAR interferometry," *Geoscience and Remote Sensing, IEEE Transactions on*, vol. 45, no. 11, pp. 3481–3493, Nov. 2007.
[36] A. Freeman and S. Durden, "A three-component scattering model for polarimetric SAR data," *Geoscience and Remote Sensing, IEEE Transactions on*, vol. 36, no. 3, pp. 963–973, May 1998.
[37] D. R. Sheen, N. L. VandenBerg, S. J. Shackman, D. L. Wiseman, L. P. Elenbogen, and R. F. Rawson, "P-3 ultra-wideband SAR: Description and examples," *IEEE AES Systems Magazine*, pp. 25–29, Nov. 1996.
[38] A. Freeman, "Fitting a two-component scattering model to polarimetric SAR data from forests," *Geoscience and Remote Sensing, IEEE Transactions on*, vol. 45, no. 8, pp. 2583–2592, Aug. 2007.
[39] K. P. Papathanassiou and S. R. Cloude, "Three-stage inversion process for polarimetric SAR interferometry," *IEE Proc. Radar Sonar Navig.*, vol. 150, pp. 125–134, Jun. 2003.
[40] S. Tebaldini, "Algebraic synthesis of forest scenarios from multibaseline polinsar data," *Geoscience and Remote Sensing, IEEE Transactions on*, vol. 47, no. 12, pp. 4132 –4142, dec. 2009.
[41] S. Cloude and E. Pottier, "A review of target decomposition theorems in radar polarimetry," *Geoscience and Remote Sensing, IEEE Transactions on*, vol. 34, no. 2, pp. 498–518, Mar 1996.
[42] C. V. Loan and N. Pitsianis, "Approximation with Kronecker products," *Linear Algebra for Large Scale and Real Time Applications, M. S. Moonen, G. H. Golub, and B. L. R. De Moor, Ed. Norwell, MA: Kluwer*, pp. 293–314, 1993.
[43] L. F. Famil and M. Neumann, "Recent advances in the derivation of pol-insar statistics: Study and applications." in *Eusar 2008*, 2008.
[44] S. Cloude and E. Pottier, "An entropy based classification scheme for land applications of polarimetric SAR," *Geoscience and Remote Sensing, IEEE Transactions on*, vol. 35, no. 1, pp. 68–78, Jan 1997.
[45] S. Tebaldini and F. Rocca, "BioSAR WP43," *ESTEC Contract No. 20755/07/NL/CB*, 2008.
[46] ——, "BioSAR 2008 Data Analysis II," *ESTEC Contract No. 22052/08/NL/CT*, 2009.

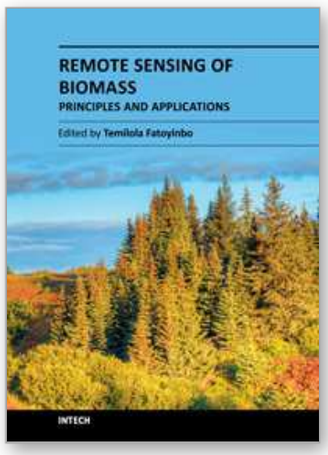

Remote Sensing of Biomass - Principles and Applications

Edited by Dr. Lola Fatoyinbo

ISBN 978-953-51-0313-4
Hard cover, 322 pages
Publisher InTech
Published online 28, March, 2012
Published in print edition March, 2012

The accurate measurement of ecosystem biomass is of great importance in scientific, resource management and energy sectors. In particular, biomass is a direct measurement of carbon storage within an ecosystem and of great importance for carbon cycle science and carbon emission mitigation. Remote Sensing is the most accurate tool for global biomass measurements because of the ability to measure large areas. Current biomass estimates are derived primarily from ground-based samples, as compiled and reported in inventories and ecosystem samples. By using remote sensing technologies, we are able to scale up the sample values and supply wall to wall mapping of biomass. Three separate remote sensing technologies are available today to measure ecosystem biomass: passive optical, radar, and lidar. There are many measurement methodologies that range from the application driven to the most technologically cutting-edge. The goal of this book is to address the newest developments in biomass measurements, sensor development, field measurements and modeling. The chapters in this book are separated into five main sections.

INTECH
open science | open minds

InTech Europe
University Campus STeP Ri
Slavka Krautzeka 83/A
51000 Rijeka, Croatia
Phone: +385 (51) 770 447
Fax: +385 (51) 686 166
www.intechopen.com

InTech China
Unit 405, Office Block, Hotel Equatorial Shanghai
No.65, Yan An Road (West), Shanghai, 200040, China
中国上海市延安西路65号上海国际贵都大饭店办公楼405单元
Phone: +86-21-62489820
Fax: +86-21-62489821

IntechOpen